J. Fluid Mech. (1971), *vol.* 45, *part* 2, *pp.* 281–319
Printed in Great Britain

A study of free jet impingement. Part 1. Mean properties of free and impinging jets

By COLEMAN DUP. DONALDSON
AND RICHARD S. SNEDEKER
Aeronautical Research Associates of Princeton, Inc., Princeton, New Jersey

(Received 12 November 1968 and in revised form 29 May 1970)

In this, the first part of a two-part experimental study of the behaviour of impinging jets, the mean properties of the flow field are established. Velocity profiles are given for three types of jet flow issuing from a circular convergent nozzle. Measured distributions of surface pressure are given which result when the jets impinge both normally and obliquely at various distances on several surface shapes. The pressure distributions are used to compute the radial velocity gradient at the impingement stagnation point. It is found that for normal impingement this gradient correlates with the free jet centreline velocity and half-radius at the same axial location. A fall-off in the correlated value is noted as the impingement is made oblique. Measurements of the azimuthal distribution of momentum flux in the resulting wall jet are also given. The general behaviour of all three types of jet is found to be similar at locations downstream of any local effects due to the shock waves present in the under-expanded types. A special study of the close-range impingement of an under-expanded jet containing a normal shock disk reveals a region of separated flow surrounding the stagnation point. This condition results in a negative value of the radial velocity gradient at the centreline.

1. Introduction

There are so many instances in nature and in engineering when the problem of free jet impingement is of importance that the task of preparing a complete list of examples, together with suitable editorial comment, is of itself a major undertaking. Such a survey will not be undertaken here. Suffice it to say that the authors of the present study were motivated primarily by a desire to understand the phenomenon of jet impingement heat transfer. In order to obtain enough information to achieve some basic understanding of this problem, a great deal of groundwork was necessary on the nature of the particular jet that was used in these investigations and its interaction with the plate on which it impinged. Some of the information gathered covers ground that has already been reported by other investigators, but a great deal of the data obtained represent new results that are thought to be most useful to the engineer. Since each free jet in its own particular laboratory has its own special idiosyncrasies, the new data obtained are best understood if complete information concerning the mean and turbulent properties of the particular jet used in these investigations is presented. In order to make this complete reporting possible within the constraints of convenient journal publication length, the present study is reported in two parts.

The principal flow investigated was a subsonic free jet produced by a simple, convergent, round nozzle. The details of the mean structure of this flow are given in the first part of the study, together with the pressure distributions and wall jets that result when the free jet impinges on a surface. The second part of the study covers the detailed turbulent structure of the free jet and the measurement of heat transfer rates produced by impingement.

To broaden the study to take into account the effects of jet strength and shock structure, measurements were also made of the mean properties and impingement characteristics of both moderately and highly under-expanded jets from the same nozzle.

Anticipating somewhat the results of these studies, it has been found that the nature of the flow in a free jet impingement can best be correlated in terms of the characteristics that the free jet would have in the plane of impingement were the impingement surface to be removed. When one is interested in the pressure distribution resulting from impingement, it is found that, as might be expected, this can be related to the local mean properties of the free jet. On the other hand, when one is interested in jet impingement heating, a knowledge of the local turbulent structure of the free jet is important. It is found, moreover, that for the case of under-expanded jets, these same correlations are valid for impingement of regions of the jet downstream of the local influence of its shock structure. Some special characteristics of the impingement of the region containing the shock structure are also reported.

The reader of either part of this overall study will find it useful to keep in mind the general notion that jet impingements are largely governed by the nature of the inviscid interaction that would occur if an inviscid jet having the properties of the real jet in the plane of impingement were to impinge on the surface in question.

2. Free jet studies

2.1. *Structure of the turbulent axially symmetric free jet*

An extensive literature on the structure of turbulent free jets exists (see, e.g. Krzywoblocki's (1956) literature survey). The bulk of this work deals with the decay of subsonic jets issuing from round nozzles into a quiescent medium. Relatively little information is available on the decay of under-expanded jets (Anderson & Johns 1955; Seddon & Haverty 1956; D'Attore & Harshbarger 1964; Owen & Thornhill 1952). Analytical and semiempirical methods for determining jet characteristics likewise have been largely restricted to subsonic and properly expanded supersonic jets. In the broad approach of the present study, however, it is of interest to determine not only the local details of the flow within the core of both subsonic and under-expanded jets, but also the effects of under-expansion on decay and spreading rates downstream. Knowledge of the latter effects, if any, should enable one to consider the problem of free jet decay and impingement in terms of a single class of flows without special regard for the under-expanded condition except, perhaps, in the core region.

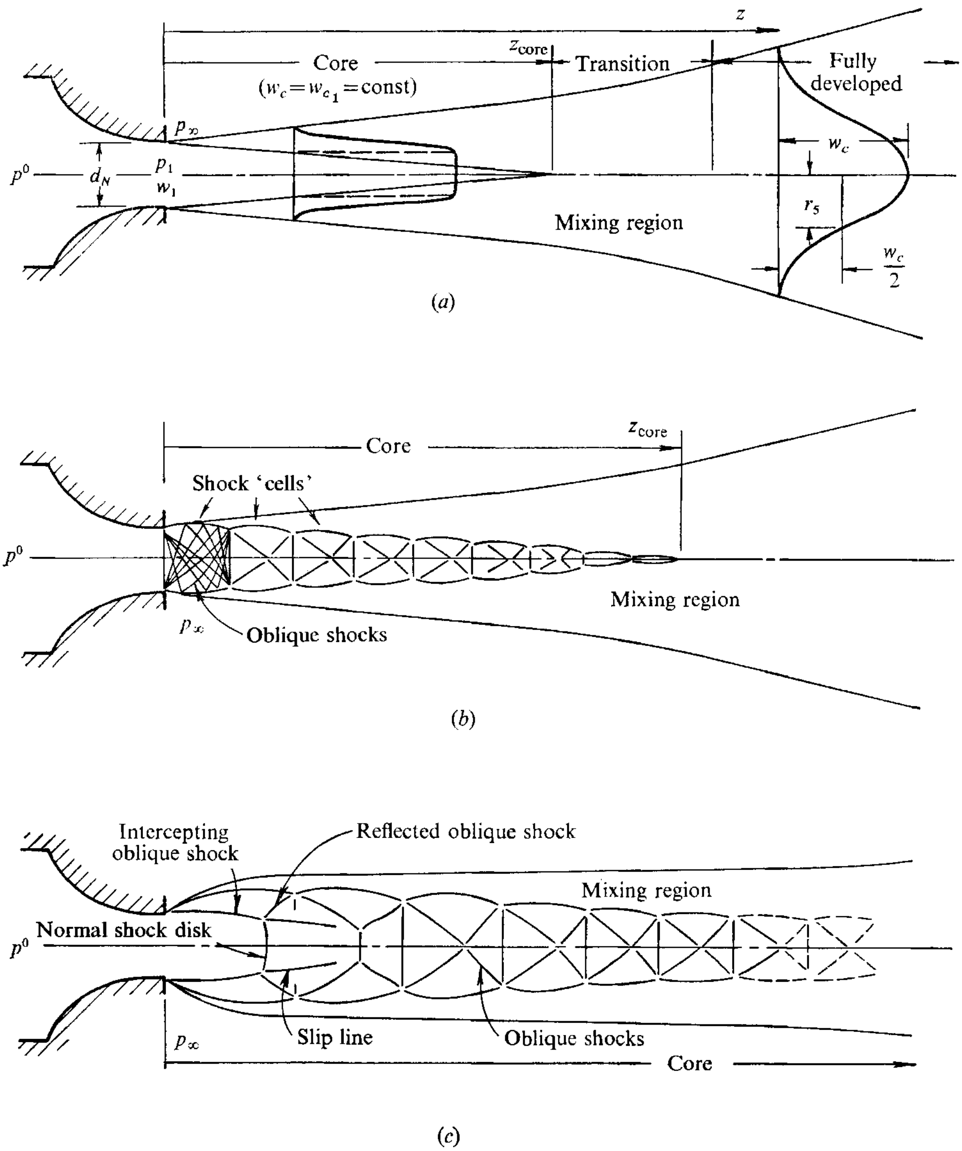

FIGURE 1. Three major variations of jet flow from a sonic nozzle. (*a*) Subsonic jet: $1 > p_\infty/p^0 > 0{\cdot}528$, $p_1/p_\infty = 1$. (*b*) Moderately under-expanded jet: $0{\cdot}48 > p_\infty/p^0 \gtrsim 0{\cdot}26$, $1{\cdot}1 < p_1/p_\infty \lesssim 2$. (*c*) Highly under-expanded jet: $0{\cdot}26 \gtrsim p_\infty/p^0 > 0$, $2 \lesssim p_1/p_\infty < \infty$.

Only recently has interest in the characteristics of rocket exhaust plumes at high altitudes and in space spurred efforts to understand structural details of under-expanded jets. Some specific problems which have been studied involve pressure, thermal and shock interference effects on adjacent structure, as well as vehicle stability effects and the blocking of communication signals due to ionization radiation in the plume. The emphasis, however, has been on the determination of initial spreading boundaries of the plume and the strength and location of the initial shock structure rather than decay processes or impingement. An extensive study of this kind has been reported by Love, Grigsby, Lee & Woodling (1959). Other recent studies have been concerned with jet applications in the fluid amplifier field (Olson & Miller 1963) and the interrelation between under-expanded jet stability and associated sound generation phenomena (Hammitt 1961).

The general structure of a turbulent free jet is well known. If we consider the flow issuing from a circular convergent nozzle, three major variations of the flow pattern are possible, depending upon the pressure ratio through the nozzle. These variations are referred to here as the subsonic jet, the moderately under-expanded jet, and the highly under-expanded jet. (Although a properly expanded Mach 1 jet can exist in principle, it is not treated in the present discussion.) The idealized structural features of each of these variations, as well as the nomenclature and symbols used to describe these jets throughout the remainder of this paper, are shown in figure 1. The pressure ratio values given are for air. Typical schlieren pictures of each jet type are shown in figure 2 (plate 1).

The subsonic jet is characterized by a potential core surrounded by a region in which mixing between jet and ambient fluid takes place. Several nozzle diameters downstream, the mixing region has spread inward enough to reach the centreline, and the core no longer exists. Beyond this point, the mixing region continues to spread as the velocity decays at a rate required to conserve axial momentum. In this portion of the jet, the mean velocity profiles approach the self-similar shape of the fully developed jet. Such a subsonic jet exists for air for isentropic pressure ratios $1 > p_\infty/p^0 > 0{\cdot}528$. Throughout this range it can be assumed that $p_1/p_\infty = 1$.

When the sonic, or critical, pressure ratio is reached, a very weak normal shock forms at the exit. This shock changes rapidly with increasing pressure ratio, however, and at $p_1/p_\infty \approx 1{\cdot}1$, the familiar pattern of 'shock diamonds' or 'cells' composed of intersecting oblique shocks is established in the core. This structure persists, for a sonic exit, until $p_1/p_\infty \approx 2$. The term 'moderately under-expanded' is used here to denote jets within this pressure ratio interval ($1{\cdot}1 \lesssim p_1/p_\infty \lesssim 2$). Because of the additional expansion required in the unconfined jet flow beyond the nozzle, the boundaries of what was the potential core in the subsonic case are now determined by the requirement of pressure equilibrium between the outermost portion of the flow within the shock structure and the surrounding ambient air. The inward diffusion of the mixing region, however, continues, and ultimately results in the dissipation of the core. Downstream of the core, after the jet has become subsonic, the spread and decay would be expected to be similar to that of a totally subsonic jet.

At a pressure ratio $p_1/p_\infty \approx 2$ (for a sonic exit), the form of the shock structure in the initial cell begins to change. Along the centreline, where the expansion is a maximum, the pressure becomes so low relative to ambient pressure that the recompression in the remainder of the cell reaches the limiting value for conical shocks, and the required compression takes place through an observable normal shock disk. Once this disk forms, the jet is said to be 'highly under-expanded'. As the pressure ratio p_1/p_∞ is further increased, the shock disk increases both in strength and diameter. Immediately downstream of the disk, the flow is subsonic. Since the surrounding flow in the oblique shock region remains supersonic, a slip line exists at the boundary between the two concentric regions. For a fairly high degree of under-expansion, say $p_1/p_\infty \approx 4$, this subsonic core region is quickly accelerated and becomes supersonic once again near the beginning of the second cell. In this case the second cell may resemble the first and even possess a normal shock similar to that in the first cell. For very high pressure ratios, the structure downstream of the first cell is dominated for a great distance by the very strong normal shock in the first cell, and no other normal shocks are present. The flow then decays through a structure of oblique shocks. The mixing region surrounds the core as usual, but its radial diffusion is small, with the result that the core of the highly under-expanded jet can be extremely long. Far downstream, the usual subsonic decay takes place.

2.2. *Experimental programme*

Since each of the three major jet variations described above was expected to exhibit an impingement behaviour somewhat different from the others, a typical case representative of each régime was chosen for detailed study. Values of radial spread and axial decay for each of these jets were used later to correlate the results of impingement measurements made using jets with these same strengths. The jets used to provide these data are as follows:

Subsonic jet:	Moderately under-expanded jet:	Highly under-expanded jet:
$p_\infty/p^0 = 0{\cdot}800$	$p_\infty/p^0 = 0{\cdot}372$	$p_\infty/p^0 = 0{\cdot}148$
$p_1/p_\infty = 1$	$p_1/p_\infty = 1{\cdot}42$	$p_1/p_\infty = 3{\cdot}57$
$M_1 = 0{\cdot}57$	$M_1 = 1$	$M_1 = 1$

2.2.1. *Apparatus and instrumentation.* A convergent nozzle with an exit diameter $d_N = 0{\cdot}511$ in. and exhausting to atmospheric pressure was used. This nozzle was mounted on a settling chamber which was supplied with air from a storage tank through an automatic regulator valve. The settling chamber and nozzle are shown in figure 3 (plate 2) which also shows the flat plate model used in the impingement studies described later.

Local velocities were computed from measured Pitot and static pressure profiles. The Pitot and static pressure probes used were made of 0·032 in. O.D. stainless-steel tubing; the Pitot tube was cut off square and the static tube was a slender ogive with two 0·0135 in. holes on opposite sides $\frac{5}{16}$ in. from the tip.

2.2.2. *Results of velocity profile and photographic studies.* For each jet, the velocity profiles and spreading and decay characteristics calculated from the pressure measurements are given in figures 4, 5, and 6. In figure 7, the spreading characteristics of all three jets are replotted together in order to emphasize certain basic differences. The velocities shown in the profiles are non-dimensionalized on the maximum velocity. The radial co-ordinate is non-dimensionalized on r_5, the radius at which the velocity drops to one-half its maximum value.

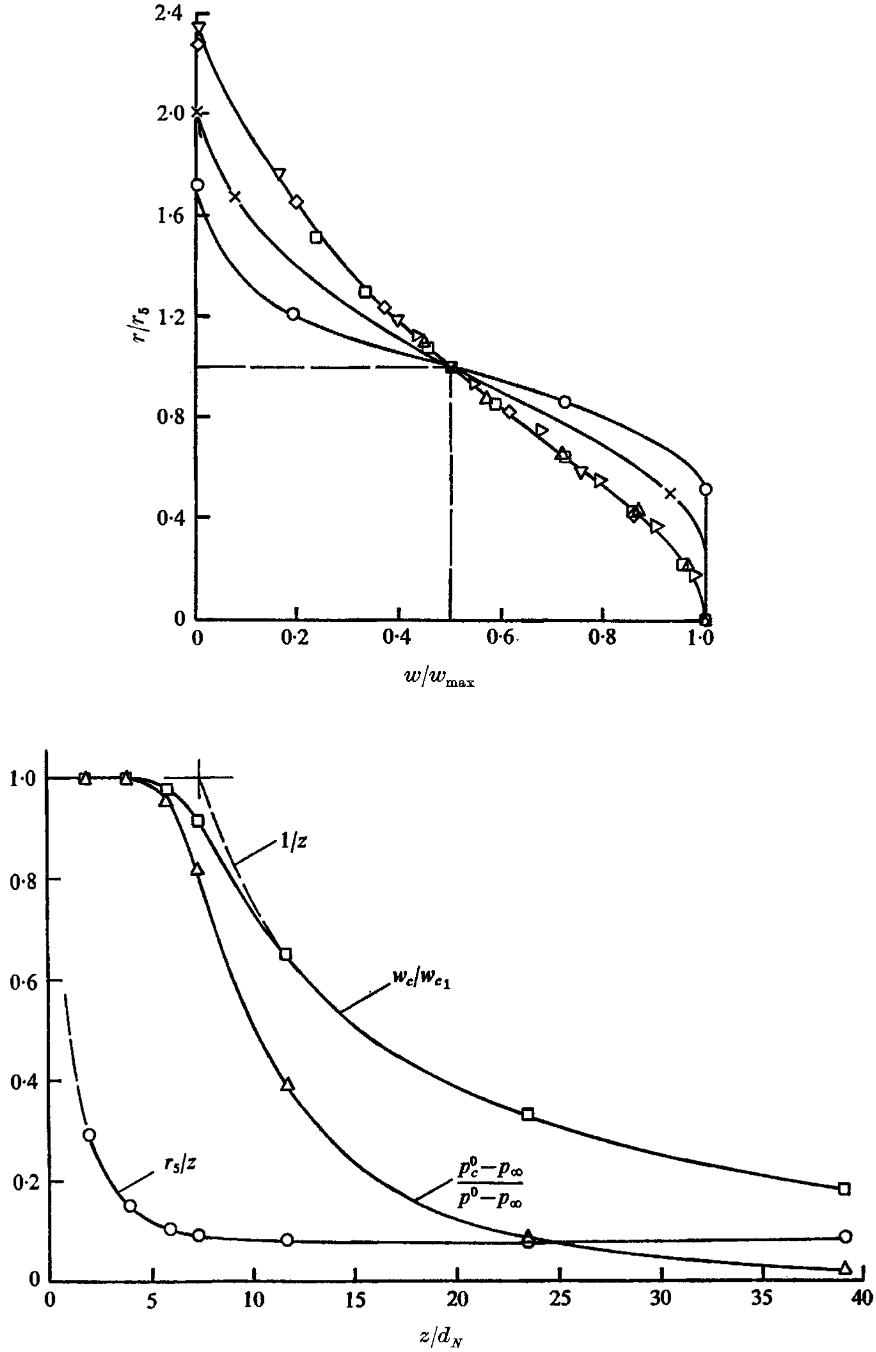

FIGURE 4. Normalized jet velocity profiles and axial decay and spreading characteristics. $p_1/p_\infty = 1{\cdot}00$; $p_\infty/p^0 = 0{\cdot}800$; $M_1 = 0{\cdot}57$; $p^0 = 17{\cdot}9$ psia. Values of z/d_N for velocity profiles: ○, 1·96; ×, 3·92; ▽, 7·32; ◇, 11·7; □, 23·5; △, 39·1; ▷, 58·7.

The velocity profiles of figure 4 show the expected structural features of the subsonic jet. The core with its profile of uniform velocity near the centreline ($z/d_N = 1{\cdot}96$ and $3{\cdot}92$) and the fully developed region with self-similar profiles

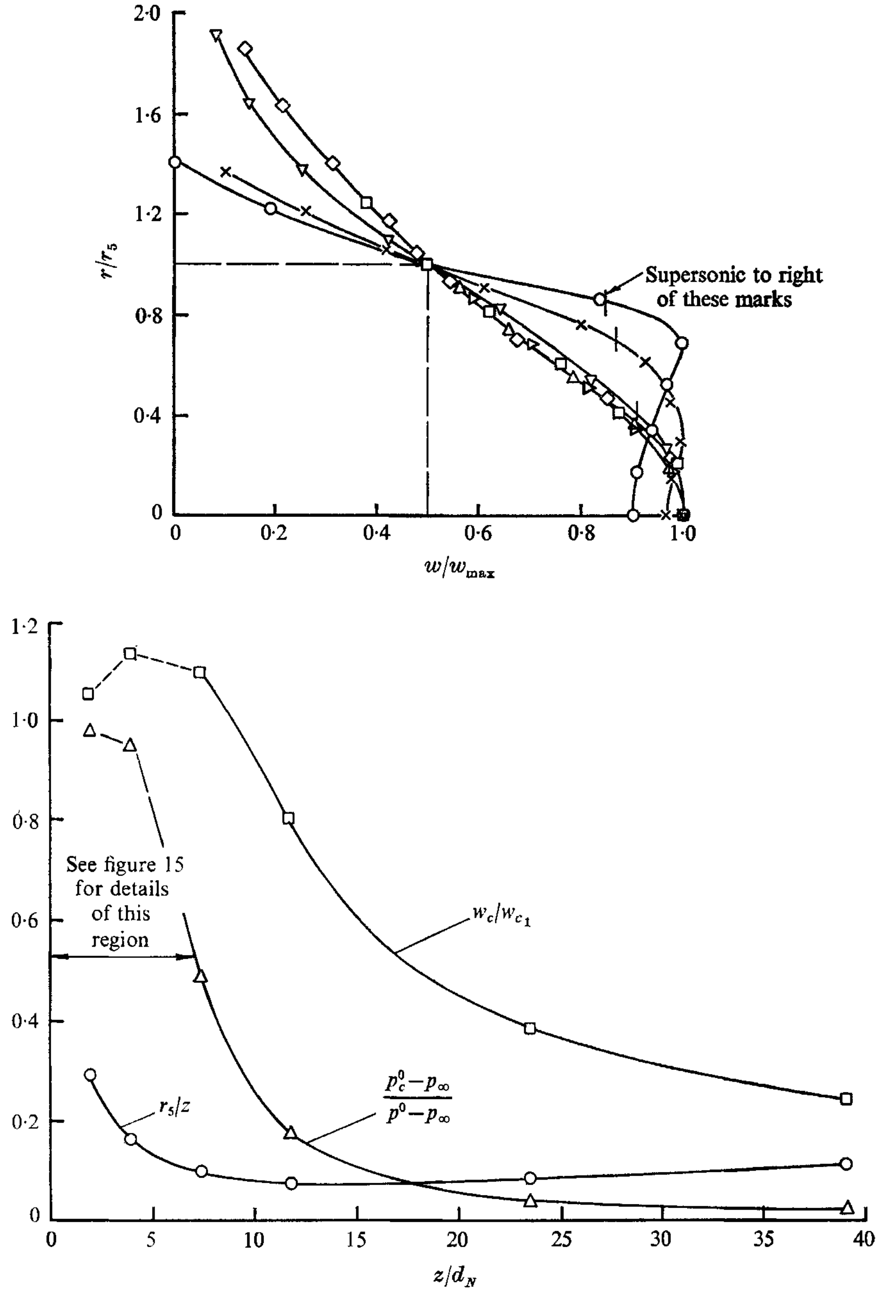

FIGURE 5. Normalized jet velocity profiles and axial decay and spreading characteristics. $p_1/p_\infty = 1{\cdot}42$; $p_\infty/p^0 = 0{\cdot}372$; $M_1 = 1{\cdot}00$; $p^0 = 39{\cdot}7$ psia. See figure 4 for definition of symbols.

(z/d_N = 11·7, 23·5, 39·1, and 58·7) have the usual appearance. Downstream of $z/d_N \approx 11$, the decay follows a characteristic incompressible $1/z$ dependence quite closely. If this curve is extended back upstream to a value of unity, neglecting the transitional region, an apparent core length z_{core}/d_N of about 7·5 is found.

For the moderately under-expanded jet (figure 5), the effects of under-

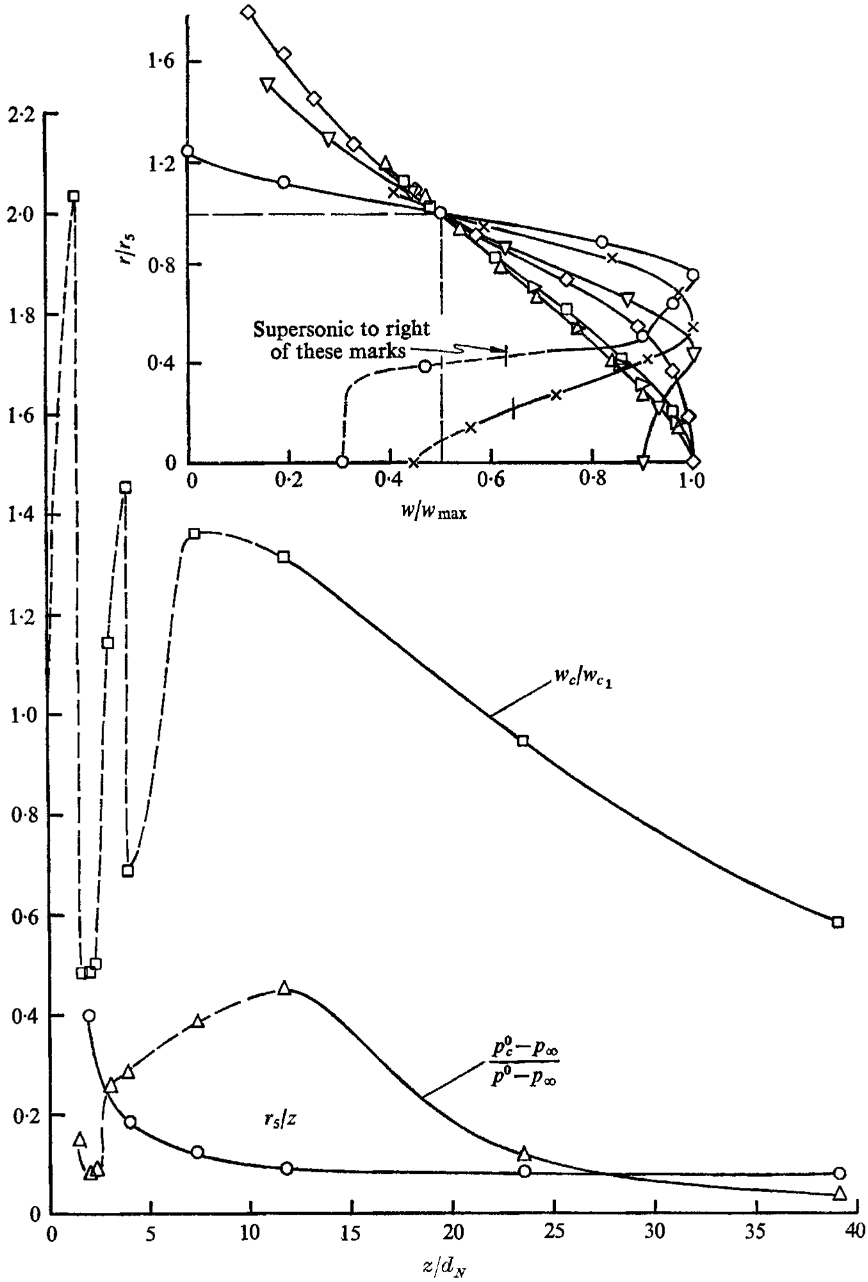

FIGURE 6. Normalized jet velocity profiles and axial decay and spreading characteristics. $p_1/p_\infty = 3{\cdot}57$; $p_\infty/p^0 = 0{\cdot}148$; $M_1 = 1{\cdot}00$; $p^0 = 99{\cdot}7$ psia. See figure 4 for definition of symbols.

expansion are at once apparent. For example, at the three points chosen for the measurements, the centreline velocity is supersonic in the core region. However, because of the local velocity variations within the length of each shock cell, these three points alone are insufficient to show the detailed core structure, and the curve through them is thus drawn dashed. The highly detailed survey of Pitot pressure shown in figure 15 is clearly indicative of the kind of axial variations to be expected in this region.

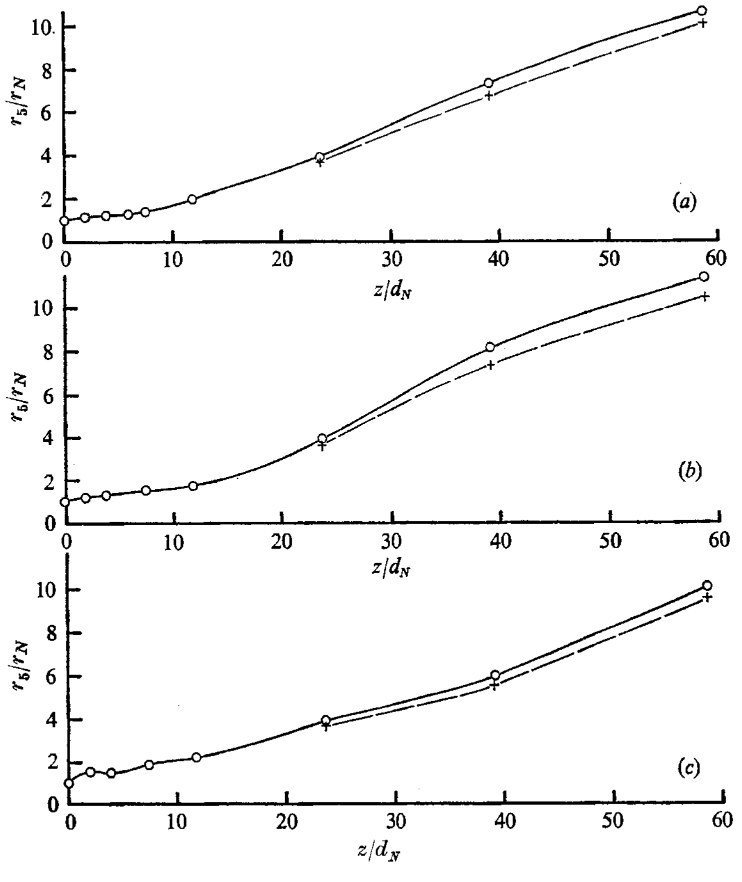

FIGURE 7. Measured radial spread of subsonic and under-expanded free jets. ——, p measured; — — —, $p = p_\infty$. (a) $p_\infty/p^0 = 0{\cdot}800, p_1/p_\infty = 1{\cdot}00$. (b) $p_\infty/p^0 = 0{\cdot}372, p_1/p_\infty = 1{\cdot}42$. (c) $p_\infty/p^0 = 0{\cdot}148, p_1/p_\infty = 3{\cdot}57$.

The velocity profiles show clearly the local effects of expansion in the core. At $z/d_N = 1{\cdot}96$, $3{\cdot}92$, and $7{\cdot}32$, for example, the central portion of the profile is seen to be supersonic. For $z/d_N = 11{\cdot}7$, the profile is subsonic throughout but still shows a slight flattening near the centreline. Fully developed subsonic profiles are observed for $z/d_N = 23{\cdot}5$, $39{\cdot}1$, and $58{\cdot}7$.

The data for the highly under-expanded jet (figure 6) show that the distinguishing feature in the upstream region is the normal shock disk. Photographs show that this shock occurs at $z/d_N = 1{\cdot}58$. Just downstream of the point, at

$z/d_N = 1{\cdot}96$, the velocity profile has the expected subsonic central region. The axial Pitot survey (figure 15) shows that the Mach number on the centreline is 3·5 just upstream of the shock and 0·45 just downstream of the shock. In the surrounding region, a peak Mach number of 1·9 is reached. The sudden loss in Pitot pressure shown in figure 15 which occurs at $z/d_N = 3{\cdot}9$ is believed to indicate a normal shock in the second cell. Correspondingly, the velocity profile at $z/d_N = 3{\cdot}92$ does show a small subsonic central portion. At $z/d_N = 7{\cdot}32$, the entire central region is supersonic, but the maximum velocity still does not occur on the centreline. In this respect, the profile is similar to some of those found in the core of the moderately under-expanded jet. A substantial supersonic core remains at $z/d_N = 11{\cdot}7$, although, at least at this specific point, the peak velocity lies on the axis. While the oblique shock structure in the region between the last normal shock and the end of the core does not consist of well-defined cells (see figure 2), it is likely that those shocks which are present will produce local fluctuations in the velocity profile as long as they are of sufficient strength. Thus, no smooth variation from profile to profile should be inferred from the data presented for this region. Farther downstream, it is observed that the centreline velocity is just subsonic at $z/d_N = 23{\cdot}5$. The detailed Pitot pressure survey (figure 15) reveals a substantial recovery of Pitot pressure relatively far downstream. This is due to the inward diffusion of momentum from the high-speed portion of the jet surrounding the low-speed core.

The velocity spread data for this jet (figure 7) reveal a somewhat erratic behaviour. In the region immediately downstream of the nozzle exit, the bulge observed is consistent with the boundary shape assumed by the expanding flow in the first few shock cells. Except for slight deviations, the spreading rate is then essentially constant for a considerable distance downstream ($z/d_N \approx 40$).

2.2.3. *Secondary effects and factors affecting profile measurements.* Jet flows, like wind tunnel flows, are subject to secondary influences arising from the unique characteristics of the particular apparatus in use. For a jet, one important effect of this kind is a flapping instability; that is, a relatively low frequency lateral oscillation of the entire flow field about its mean location. All turbulent jets flap to some extent under the proper conditions, but a given jet may flap more or less when slight changes are made in the conditions under which it forms. Another important secondary effect is that due to interference from obstructions in the entrained flow field. Obstructions can alter the spreading and decay of a jet as well as its direction, cross-sectional shape, and momentum distribution. It is because of such interference that a jet issuing from a hole in a plane surface exhibits a higher rate of spread and decay than does one issuing from the end of a long pipe. An example of the magnitude of secondary effects is found in a comparison of the measured core length of the subsonic jet with the results of Warren (1957). In the present case, a length $z_{\text{core}}/d_N = 7{\cdot}5$ was found for $M_1 = 0{\cdot}57$. For $M_1 = 0{\cdot}69$, Warren found $z_{\text{core}}/d_N = 7{\cdot}2$. Since this shorter core length with a higher Mach number is in contradiction with the usually observed core length-Mach number dependence, and since the measurement techniques were the same, it is likely that differences in the secondary factors account for this anomaly.

To illustrate the nature of the jet flapping instability, a series of continuous light schlieren pictures was taken using a high sensitivity double-pass coincident optical system. The jet pressure ratio p_1/p_∞ was varied in small increments through a range from 1·00 to more than 4. In figure 8 (plate 3), a selection of these pictures is shown. It is observed that an intensified image of the mixing region is obtained. Because of the relatively long exposure time ($\frac{1}{50}$ sec), this image is representative of the time average appearance. It is at once apparent that there is considerable variation of the observed spread of the jet as the pressure ratio is changed. This variation is interpreted as being due to changes in the magnitude of flapping of the entire jet flow field. As the pressure ratio is increased, two distinct ranges are noted in which the instability appears to be very intense. An increase of pressure ratio from 1·15 to 1·42 and then further to 1·59 spans the first such range with the $p_1/p_\infty = 1{\cdot}59$ case appearing to be relatively stable. A second range of even greater instability seems to centre about the case for $p_1/p_\infty = 1{\cdot}84$. At a pressure ratio of 2·00, the normal shock disk is first observed. Within the region covered by the pictures, the degree of instability appears to lessen with further increases in pressure ratio above 2. It should be emphasized that these particular changes in flapping characteristics with pressure ratio are unique for the jet apparatus used and should be thought of only as indicative of changes that can occur in any jet.

In addition to producing changes in the flow field, secondary effects also influence the accuracy of measurements in such flows. The velocity profiles upon which the spreading and decay results are based were determined from measurements made with Pitot and static pressure probes. Such measurements are affected not only by the jet flapping instability, but also by the turbulence.

The pressure sensed by a static pressure orifice is affected by any disturbance which produces a transverse velocity component. The magnitude and sign of the resulting error, however, depend on a complex relationship among probe size, turbulence scale, and the magnitude and space correlation of local velocity fluctuations. In general, therefore, the validity of the static pressure measurements can be assumed to be the greatest in regions of the jet where turbulence and instability are the least relative to the magnitude of the mean motion, namely, in the upstream regions.

In many cases, jet velocity profiles are determined from the measurement of Pitot pressures alone, with the static pressure considered to be constant and equal to ambient pressure. In the present experiments, in which static pressures were measured, it is possible to compare profile parameters determined in both ways. In figure 7, values of the spreading parameter based on ambient static pressure are shown for several cases. It is seen that a somewhat larger spreading rate results when measured static pressures are used. It is not possible, however, to determine the degree to which these measured pressures actually contribute to the determination of a true profile because the measurements are most in doubt where they can have the greatest influence, i.e. in the outer portion of the downstream region where they approach the magnitude of the total pressure level.

While total or Pitot pressure measurements are also affected by turbulent velocity components, it is felt that overall jet instability or flapping effects may be of greater importance in some of the present cases. In such cases, the response of the Pitot tube at each point in the profile can be considered to be that resulting from a fluctuating mean velocity at that point. If it is assumed that this response represents the time-average value of the fluctuation, a typical jet mixing profile measured in this way will differ from its instantaneous shape. Assuming a lateral disturbance motion whose mean amplitude is distributed axisymmetrically, the measured profile would appear to be somewhat flattened at the centre and spread out at the edges. Spreading and decay rates based on such time-average profiles would, of course, be larger than those based on instantaneous profiles.

Because of the foregoing factors, it is clear that the measurement, for example, of a high spreading rate for a given jet may only be indicative of the fact that the jet is flapping strongly. This flapping would then have to be either eliminated or evaluated by other means before the true turbulent spreading rate could be determined.

2.3. *Concluding remarks on free jet studies*

The main objective of the foregoing study of free jet properties has been the determination of spreading and decay characteristics to be used to correlate the results of impingement experiments using the same jet apparatus. By using such data in this way, the influence on the correlation of secondary effects, such as jet instability, might be expected to be minimized. Also of interest in this study has been the general behaviour and structure of free jets themselves, especially cases in which the jet is under-expanded.

The results of the three typical cases confirm the expected similarities as well as important differences among the basic flow types. In the core region of each jet, the differences are most in evidence, with the characteristic shock structure of the under-expanded jets having a strong local influence. It is found that the most useful way to compare the lengths of the cores of these jets is in terms of the point at which the mean velocity profiles characteristic of fully developed turbulent mixing are observed.

Using the measured mean velocity profiles by themselves, it is found that the subsonic jet can be considered fully developed somewhere between $z/d_N = 7{\cdot}32$ and 11·7. The moderately under-expanded jet ($p_1/p_\infty = 1{\cdot}42$), however, exhibits a profile at $z/d_N = 11{\cdot}7$ that still does not match those far downstream. It has been pointed out (see figure 8) that this particular jet appears to be quite unstable and that measured velocity profiles may represent a substantial distortion of the actual instantaneous profile. Because of this, the definition of a fully developed region is difficult. It is seen, for example, that the velocity profiles are very close to being similar for $z/d_N = 23{\cdot}5$, 39·1, and 58·7, while at the same time there is a marked decrease in the spreading rate in the same range. This situation could result if the amplitude of jet flapping were stronger in the upstream region and thus resulted in broader measured profiles there. The highly under-expanded jet is obviously dominated by a very long supersonic core, as shown by the low initial spreading rate and the centreline Mach numbers. It is doubtful, in fact, that a fully developed region occurs at all within the range of the measurements. Velocity profiles for $z/d_N = 39{\cdot}1$ and 58·7 are essentially similar, but the spreading angle (divergence angle of the locus of r_5) between these points is higher (6·0°) than that usually associated with a fully developed, three-dimensional, subsonic mixing region (about 5·0°). Of course, the apparently high spreading rate could be due to flapping in that region of the jet.

3. Impingement studies

3.1. *Basic flow characteristics*

Recent interest in ground effects machines, V/STOL aircraft, and the vertical launching and landing of rockets has led to a number of studies of various aspects of the jet impingement problem. In addition, there has been increased study of certain industrial processes involving heating by impinging hot jets and flames. In the ground effects and V/STOL field, the need to understand impingement processes has arisen not only with regard to increasing the vehicle's lifting effectiveness while in ground proximity, but also in connexion with downwash erosion effects on the ground below. Study of ground erosion effects has also been extended to the problem of landing rockets on lunar and planetary surfaces. Problems associated with the impingement and deflexion of rocket exhausts and the resulting loading of adjacent surfaces have been treated both theoretically and experimentally. The basic problem of determining heat transfer between surfaces and impinging jet flows has also been investigated in a variety of ways. Other investigators have emphasized the basic aspects of flow processes involved in impingement, as well as certain special problems such as noise generation. A bibliography of representative papers on these subjects is included in Snedeker & Donaldson (1964). Very few investigations, however, have been concerned with the impingement of under-expanded jets. Of these few, only Anderson, Johns & Hawkes (1954), Henderson (1960) and Stitt (1961) represent cases which have a close bearing on the present problem. In Anderson *et al.* (1954), the exhaust from a rocket engine was impinged on a flat surface at small impingement angles ($\alpha \leqslant 90°$), and a limited number of velocity profiles were measured in the resulting deflected jet. A more pertinent set of measurements is to be found in Henderson (1960) wherein air jets of several supersonic Mach numbers were impinged upon a circular flat plate. Pressure distributions on the plate surface were measured for a wide range of impingement angles at several axial locations in the jet. Air jets from several under-expanded supersonic nozzles were used in Stitt (1961) for a study of interaction effects on a simulated lunar surface. Limited data for slightly oblique impingement cases are included.

The flow field produced by the impingement of a turbulent, axially symmetric air jet against a surface whose diameter is large compared to that of the jet is conveniently described in terms of three flow régimes as follows: (1) the free jet régime upstream of any strong local interaction effects due to impingement; (2) the impingement régime where the strong, essentially inviscid, interaction of the jet with the impingement surface produces a change in flow direction; (3) the wall jet régime consisting of essentially radial flow along the surface beyond the point at which the strong interactions of impingement cause any local effects.

Although these three régimes can be considered separately, they are not independent; even the flow leaving the plate edge in the wall jet determines to some extent the distribution of the impinging jet entrainment flow, especially when the entire region is closely confined by solid boundaries. The flow régimes are illustrated schematically in figure 9 which also serves to define the quantities of interest.

In order to calculate the heat transfer at the stagnation point of an impinging flow, one parameter which must be evaluated (as will be discussed in part 2 of this study) is the local radial velocity gradient $(du_e/dr)_{r=0}$. This can be done experimentally by relating this gradient to the static pressure distribution on the surface in the immediate vicinity of the stagnation point. Assuming the flow outside the boundary layer to be locally incompressible, this relationship may be written

$$\left(\frac{du_e}{dr}\right)_{r=0} = \left[-\frac{1}{\rho_e}\left(\frac{\partial^2 p}{\partial r^2}\right)_{r=0}\right]^{\frac{1}{2}}, \tag{1}$$

where u_e is the velocity at the edge of the boundary layer in the deflected flow and ρ_e is the local density (see, for example, Reshotko & Cohen 1955). When the impingement is oblique ($\alpha < 90^\circ$), however, a true stagnation point heat transfer cannot be represented by the value of $(du_e/dr)_{r=0}$ measured along a single diameter, since there is an azimuthal variation of the pressure distribution upon which this gradient depends. In the present study, values of $(du_e/dr)_{r=0}$ were determined for oblique impingement, but since they were based on pressure gradients along a single diameter—that normal to the tilt axis—they are designated as $[(du_e/dr)_{r=0}]_1$ to distinguish them from axisymmetric values.

The complete description of heat transfer effects at points away from the stagnation point also requires that the azimuthal distributions of momentum and energy flux in the resulting radial wall jet be known. In the experimental programme about to be described, the wall jet flux distributions were found from velocity profiles measured at a number of points along the perimeter of the impingement surface. The full results of the impingement experiments are reported in Snedeker & Donaldson (1964, 1965).

3.2. *Experimental programme*

The experimental programme was devoted to a study of the impingement of the same three jets described earlier. Each of these jets was impinged upon a circular flat plate at various distances from the nozzle and at various angles α. The stagnation region pressure distributions were then determined, and from them the stagnation point radial velocity gradients were computed. In addition, the effect of the shape of the impingement surface was investigated by impinging the jet on a convex hemisphere, a concave hemisphere, and a cylindrical cup. These latter measurements were confined to $\alpha = 90^\circ$.

3.2.1. *Apparatus and instrumentation.* Except for the impingement models themselves, the test setup was exactly the same as that used for the free jet studies. In figure 3 (plate 2), the nozzle is shown with the flat plate model mounted in position.

All of the impingement models were made with the same wetted diameter, i.e. the distance along the impingement surface from edge to edge through the centre. This distance was 9·42 in. The individual model shapes are shown in figures 9 and 10. The flat plate and cup models were machined from aluminium and brass, respectively, while the hemispheres were of moulded epoxy and fibreglass. Numerous pressure tap holes were drilled along the horizontal and vertical diameters, with each model having four closely spaced ($\frac{1}{16}$ in.) holes along the vertical diameter near the stagnation point.

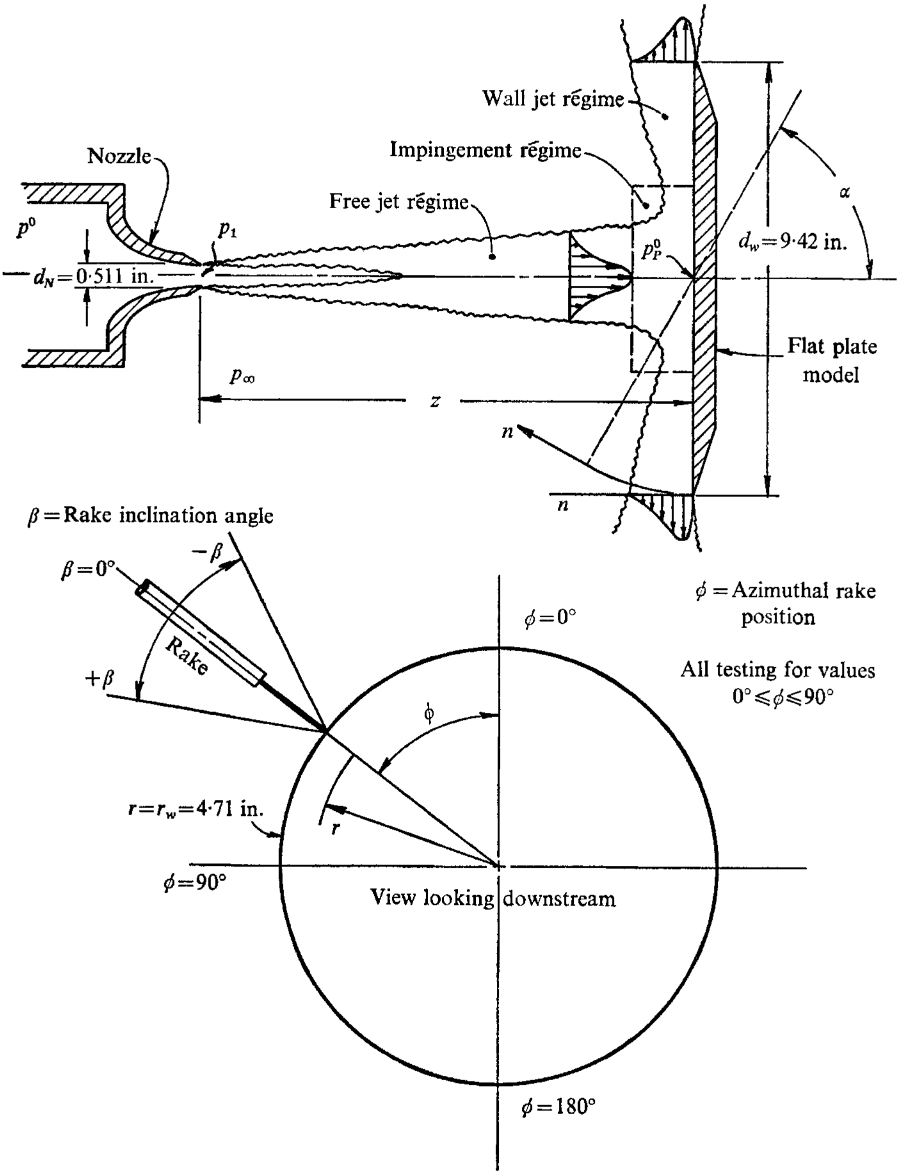

FIGURE 9. Schematic view of impingement flow with flat plate model in place.

To determine the azimuthal distribution of the wall jet, velocity profiles were measured at the edge of the plate with a Pitot tube rake. A screw adjustment provided travel of the rake in a direction n normal to the plate surface and, in addition, it was possible to pivot the rake about a line through the tips of the Pitot tubes so that an accurate measure could be made of any flow leaving the plate in a non-radial direction. In order to determine the true direction of any such non-radial flow, a direction-sensitive, wedge-type probe was mounted at one end of the rake.

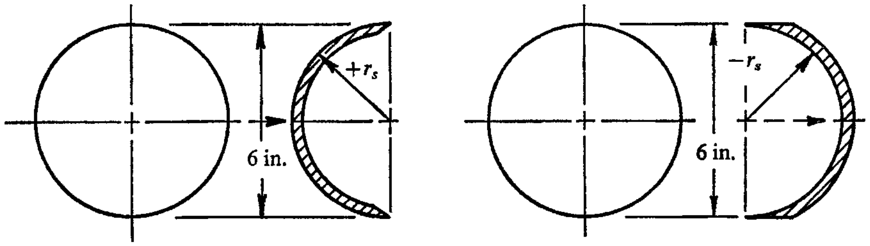

Convex hemisphere

Concave hemisphere

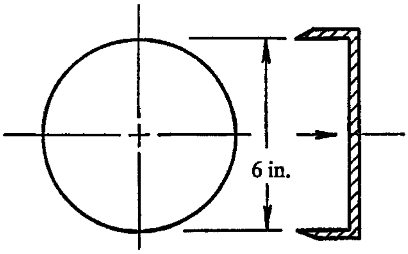

Cylindrical cup

FIGURE 10. Basic impingement model shapes.

3.2.2. *Results of pressure distribution measurements: normal impingement.* For a number of combinations of jet strength and impingement distance, pressure distributions were measured for each model. Examples of the measurements near the stagnation point are shown for several of the basic impingement conditions in figures 11, 12, and 13. On these plots, the pressure is given as a ratio of local to stagnation point absolute value, while the radial distance is given in nozzle radii from the stagnation point. In order to show clearly the differences between the distributions for different surface shapes, the data points have been omitted. For reference, the Pitot pressure profile of the free jet at the same axial location is also plotted.

It is observed that the pressure distributions follow the general local character of the free jet although there is a tendency for the impingement distribution to be relatively spread out. The case involving the highly under-expanded jet (figure 13) shows apparent stagnation points to either side of the centre with a relatively flat distribution or a third peak at the centre. The consequences of this behaviour have been investigated further and are discussed later. A consistent trend is that due to surface shape. The convex hemisphere distributions always drop off more rapidly than those of the flat plate, while those for the concave shapes drop off less rapidly.

Typical sets of overall pressure distributions, measured from edge to edge across the vertical wetted diameter of the model are shown in figure 14. The effect of distance is as might be expected, with the pressure distribution following

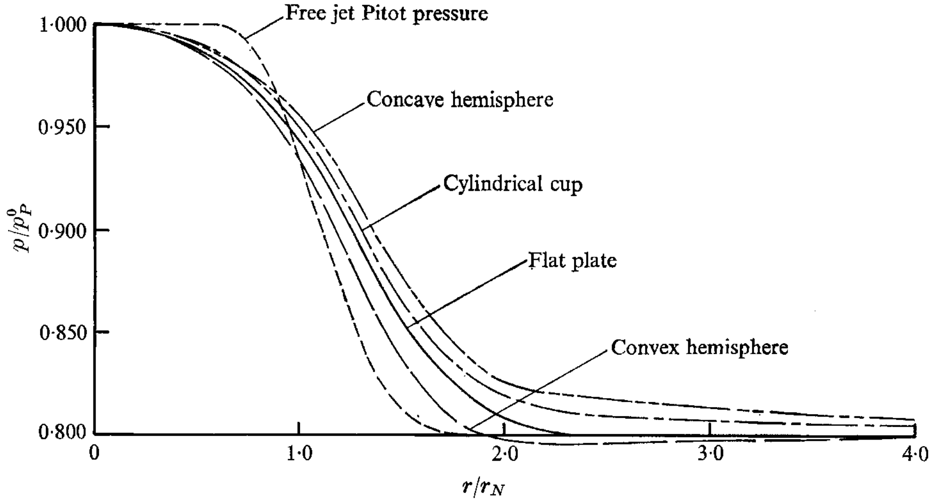

FIGURE 11. Comparison of measured stagnation region pressure distributions for several surface shapes. $z/d_N = 1·96$; $\alpha = 90°$; $p_\infty/p^0 = 0·800$; $p_1/p_\infty = 1·00$.

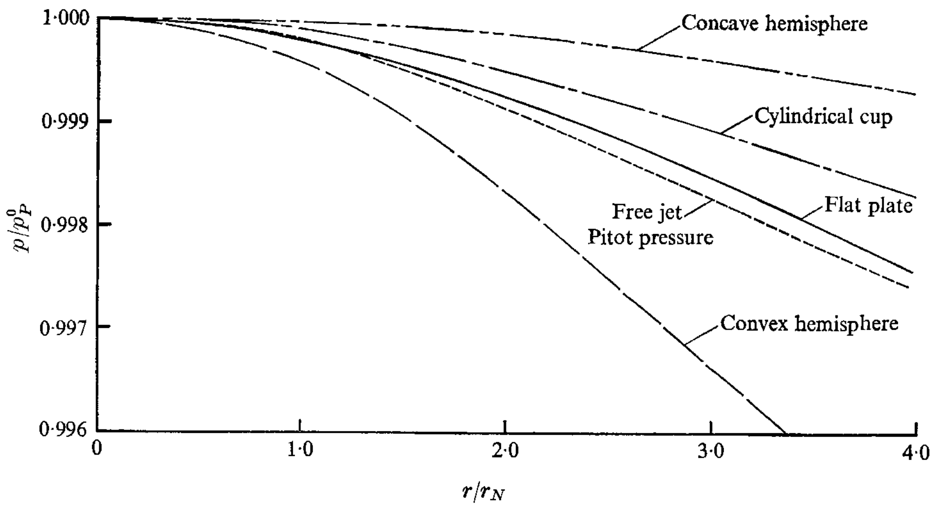

FIGURE 12. Comparison of measured stagnation region pressure distributions for several surface shapes. $z/d_N = 39·1$; $\alpha = 90°$; $p_\infty/p^0 = 0·800$; $p_1/p_\infty = 1·00$.

the basic spreading trends of the free jet. Certain details, however, are apparent which are not observed in the free jet data. In particular, some cases show a distinct reversal of the radial pressure gradient in a short interval between 2 and 3 nozzle radii from the stagnation point. This reversal has been found to depend to some extent on the surface shape, being strongest for the convex hemisphere. Since it occurs for this shape even for subsonic impingement, it appears not to be associated specifically with jet under-expansion. Whether or not the reversed gradient is sufficient to cause local separation is impossible to determine from these data alone. The behaviour of the concave shapes (e.g. figure 14(*b*)) for impingement far downstream shows that the entire flow inside these shapes approaches a stagnation condition when the jet has spread to a size comparable to that of the model.

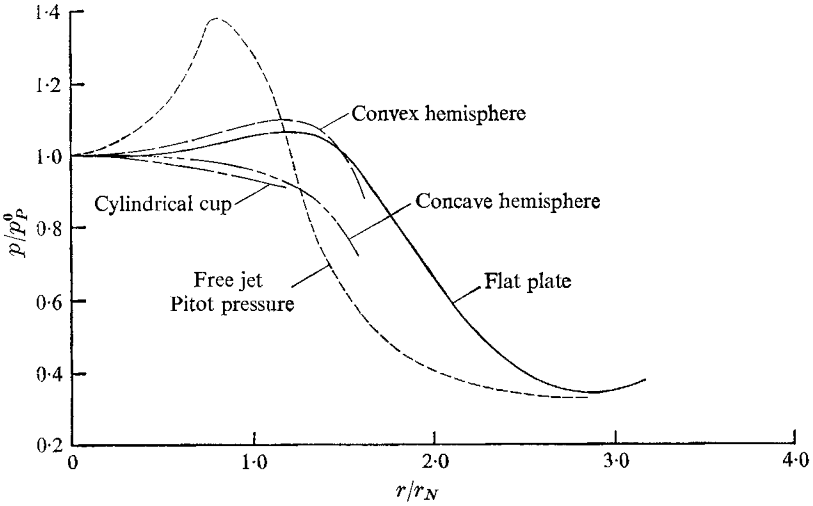

FIGURE 13. Comparison of measured stagnation region pressure distributions for several surface shapes. $z/d_N = 7{\cdot}32$; $\alpha = 90°$; $p_\infty/p^0 = 0{\cdot}148$; $p_1/p_\infty = 3{\cdot}57$.

The results of a highly detailed axial survey of the pressure at the centre of the flat plate model are given in figure 15. Also plotted is a similar survey of the Pitot pressure at the centre of each free jet. The data points for the free jet have been omitted for clarity, a measurement having been made at intervals of 0·2 nozzle diameters through most of the range $0 \leqslant z/d_N < 10$. For the subsonic case, as might be expected, the curves as plotted cannot be separated. Both of the under-expanded cases reveal the degree to which small local changes due to shock structure are duplicated in two kinds of measurement. Of particular interest is the large total pressure loss associated with the first normal shock in the highly under-expanded case. Some recovery takes place before the second normal shock and a substantial recovery is observed farther downstream where inward diffusion of momentum gradually overcomes the shock loss effect. The most important difference observed between the free jet and impingement data is an axial shift such that the plate experiences a pressure which actually occurs in the free jet at a point upstream of the plate location. This shift is thought to be primarily the result of the different stand-off distances of the impingement normal shocks. Since for a given Mach number the stand-off distance of a normal shock increases with the effective bluntness of the body, it is clear that the Pitot probe stand-off distance must be considerably less than that for the plate.

3.2.3. *Results of pressure distribution measurements: oblique impingement.* Pressure distributions were measured for oblique impingement on the flat plate model with each of the jets for several axial locations and impingement angles.

Typical pressure distributions are presented in figures 16 and 17. The pressures are given in the form of a coefficient referred to the stagnation point pressure for normal impingement, i.e.

$$\tilde{P} = \frac{p - p_\infty}{(p^0_P)_{90^\circ} - p_\infty}.$$

These distributions show clearly the expected shift in the position of the stagnation point with decreasing α as well as the changes in magnitude and shape.

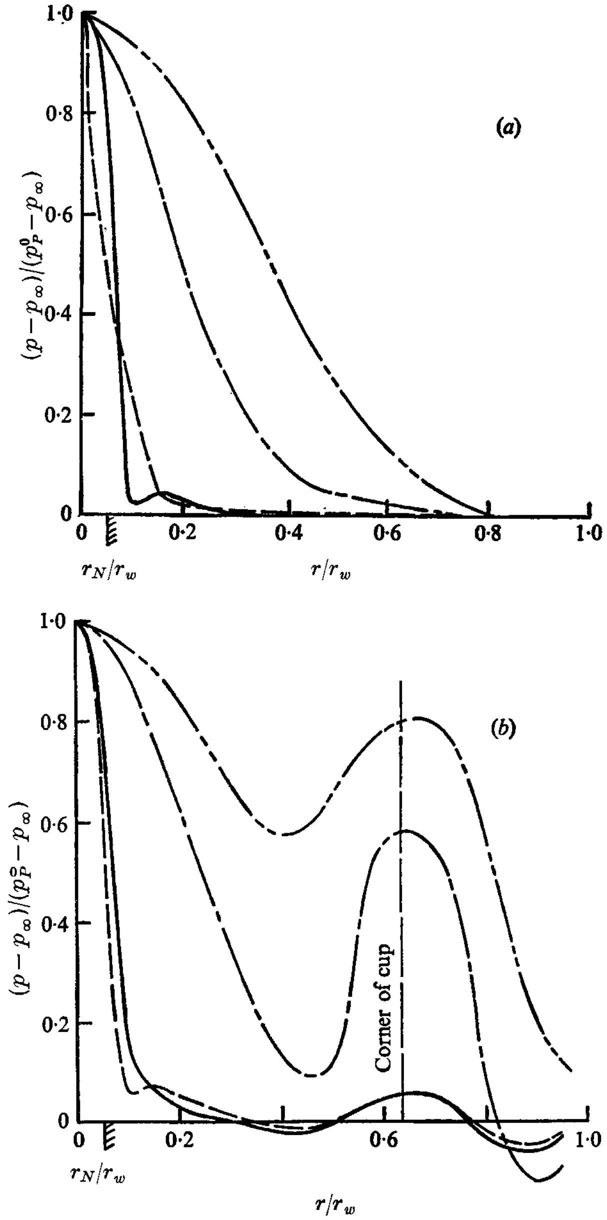

FIGURE 14. Measured overall pressure distributions. Values of z/d_N: ——, 1·96; — — —, 7·32; —·—, 23·5; —··—, 39·1. (*a*) Flat plate, $p_1/p_\infty = 1{\cdot}42$. (*b*) Cylindrical cup, $p_1/p_\infty = 1{\cdot}42$.

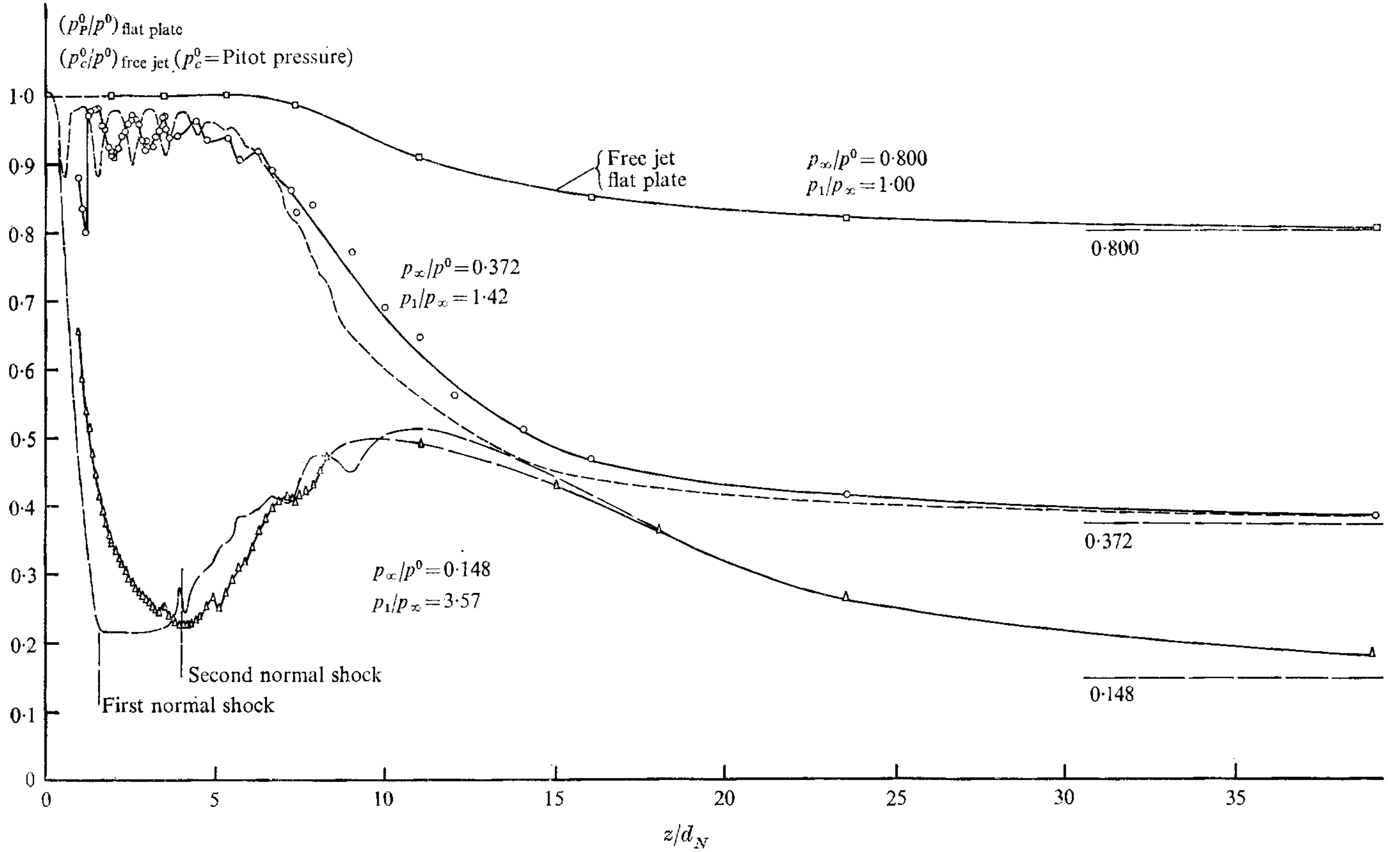

FIGURE 15. Comparison of pressures at centre of flat plate model with Pitot pressures on free jet centreline. $\alpha = 90°$. ——, flat plate; — —, free jet.

The behaviour of the pressure at the stagnation point and its position are summarized in figures 18 to 23. The stagnation point pressure increment is shown in figures 18, 19, and 20 as a fraction of its value for $\alpha = 90°$. It is seen that the behaviour is similar for all cases except when $z/d_N = 1{\cdot}96$. The near independence of axial location exhibited for the three downstream cases suggests that the behaviour is related to the free jet velocity profiles which approach self-similarity in that region. It is probable that the insensitivity to α shown for $z/d_N = 1{\cdot}96$ is associated with the relatively flat jet velocity profiles found in the core. An interesting comparison that can be made is one based on momentum considerations. Neglecting viscous effects, the force normal to the plate surface is that due to the normal component of impinging jet momentum flux, which, for a given case, is merely proportional to the integral over the surface of the square of the normal components of the impinging velocity profile. For a known profile shape, the force is thus proportional to $w^2 \sin^2 \alpha$, which, in turn, is a measure of the normal component of impinging dynamic pressure. Since the quantity $p_P^0 - p_\infty$ is also a measure of this dynamic pressure, a curve of the function $\sin^2 \alpha$ might be expected to show a close similarity with the measured values of $p_P^0 - p_\infty$. This curve is shown in figures 18, 19, and 20 for comparison.

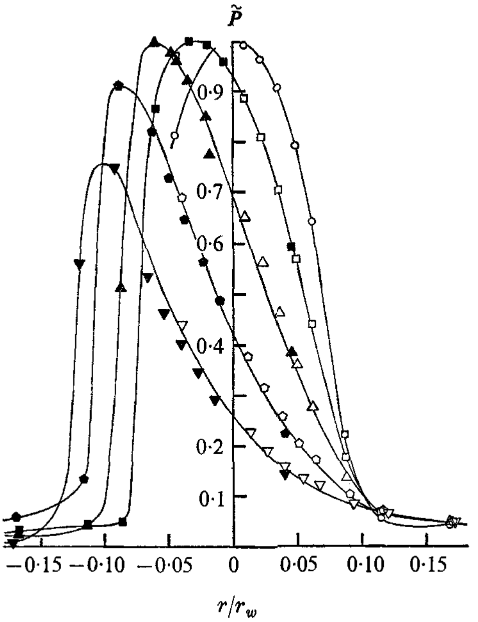

FIGURE 16

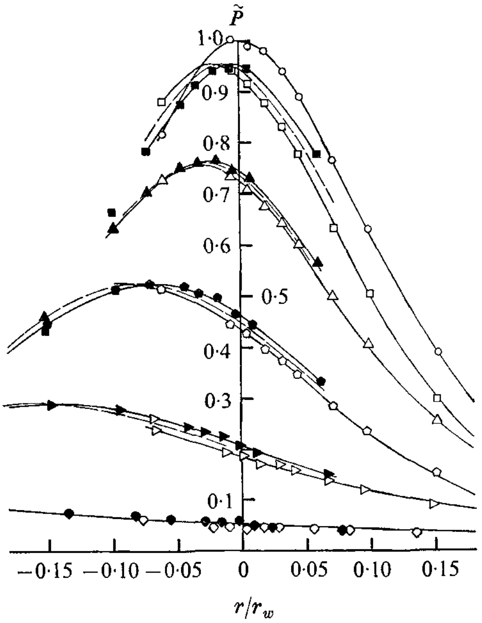

FIGURE 17

FIGURE 16. Pressure distribution on flat plate near the point of impingement. $z/d_N = 1{\cdot}96$; $p_\infty/p^0 = 0{\cdot}800$. Values of α in degrees: ○, 90; ■, □, 75; ▲, △, 60; ⬟, ⬠, 45; ▼, ▽, 35; ▶, ▷, 30; ♦, ♢, 15.

FIGURE 17. Pressure distribution on flat plate near the point of impingement. $z/d_N = 23{\cdot}5$; $p_\infty/p^0 = 0{\cdot}148$.

The displacement Δr of the stagnation point can also be referred to a normalizing parameter. In this case, the measured free jet half-velocity radius r_5 at the same axial station is used. Plots of $\Delta r/r_5$ *vs.* α are given in figures 21, 22, and 23. It is seen that except for the close impingement case ($z/d_N = 1{\cdot}96$) there is a tendency for this non-dimensional displacement also to be independent of axial distance.

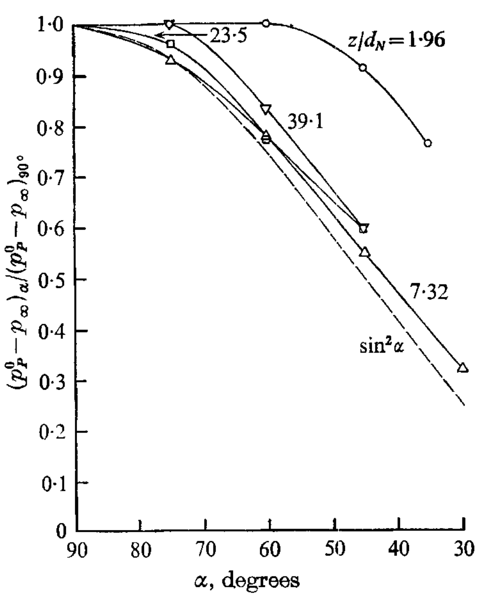

Figure 18. Dependence of non-dimensional stagnation point pressure on angle of impingement. $p_\infty/p^0 = 0{\cdot}800$.

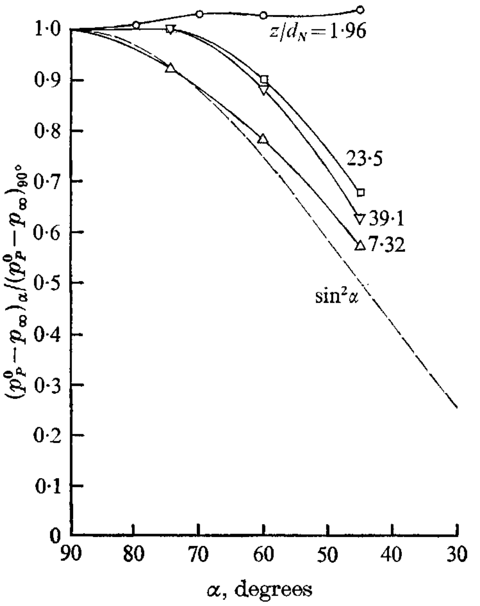

Figure 19. Dependence of non-dimensional stagnation point pressure on angle of impingement. $p_\infty/p^0 = 0{\cdot}372$.

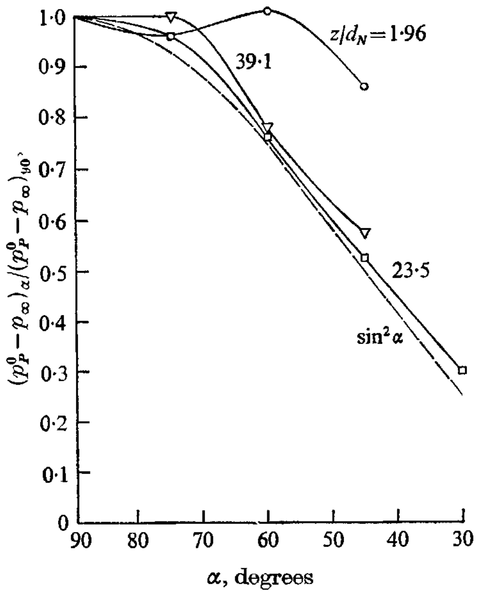

Figure 20. Dependence of non-dimensional stagnation point pressure on angle of impingement. $p_\infty/p^0 = 0{\cdot}148$.

Once again, a relationship with the local character of the free jet velocity profile is suggested, with the distance-independent cases confined to regions where the profiles are of similar shape. In contrast to the relative insensitivity to α shown by the stagnation pressure for $z/d_N = 1{\cdot}96$, the displacement Δr for this case shows the most sensitivity of all to α.

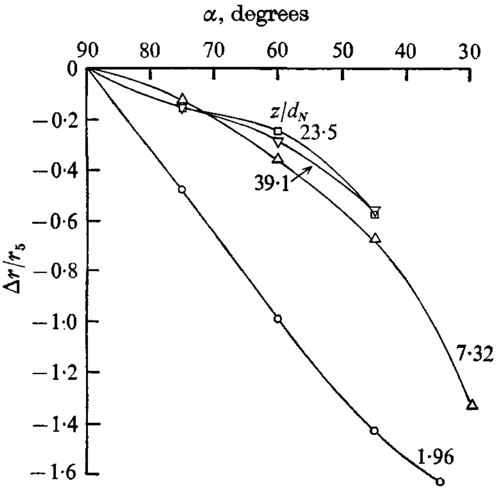

FIGURE 21. Dependence of non-dimensional displacement of stagnation point on angle of impingement. $p_\infty/p^0 = 0{\cdot}800$.

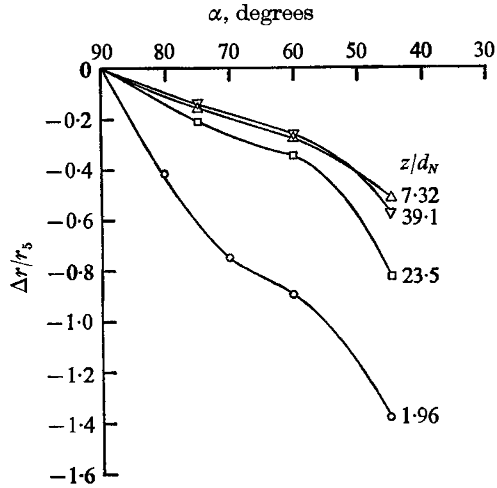

FIGURE 22. Dependence of non-dimensional displacement of stagnation point on angle of impingement. $p_\infty/p^0 = 0{\cdot}372$.

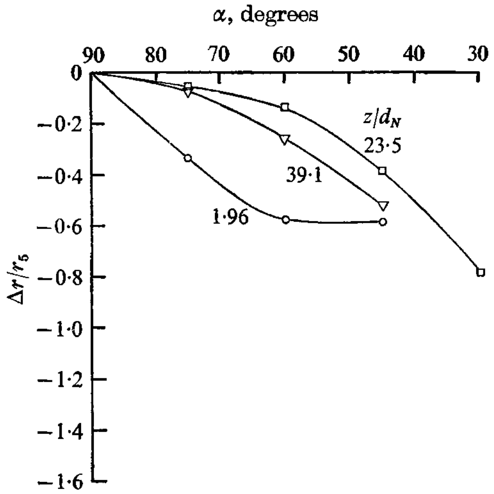

FIGURE 23. Dependence of non-dimensional displacement of stagnation point on angle of impingement. $p_\infty/p^0 = 0{\cdot}148$.

3.2.4. *Evaluation of stagnation point radial velocity gradient.* The stagnation point radial velocity gradient $(du_e/dr)_{r=0}$ was evaluated from the detailed stagnation region pressure distributions in the manner described earlier. The calculations were made by fitting the data to (1) at the stagnation point. The values were then non-dimensionalized in two ways. The first way is based on conditions at the nozzle exit, so that $(du_e/dr)_{r=0}$ has the non-dimensional form

$$\frac{d_N}{w_1}\left(\frac{du_e}{dr}\right)_{r=0}.$$

The second way, which is more fundamental but which requires a knowledge of the decay and spread of the free jet, is based on the measured local free jet conditions in the plane of impingement, i.e.

$$\frac{r_5}{w_c}\left(\frac{du_e}{dr}\right)_{r=0}.$$

Using data for the flat plate model under normal impingement, these non-dimensional forms are illustrated in figure 24 and 25. The behaviour of the values based on nozzle exit conditions is similar for the two weakest jets. This similarity is indicative of the roughly equivalent core lengths and rates of decay as well as rather weak overall effects due to shock patterns. For the highly under-expanded case, however, the behaviour is quite different, with the effects of the much longer core region and strong shock structure clearly shown. In particular, note the negative values which are associated with the reversed pressure gradient observed near the centreline for impingement downstream of the normal shock disk. Results similar to those for the flat plate were obtained for the other surface shapes, but the magnitudes were different as might be expected from the relative curvatures shown in figures 11, 12, and 13.

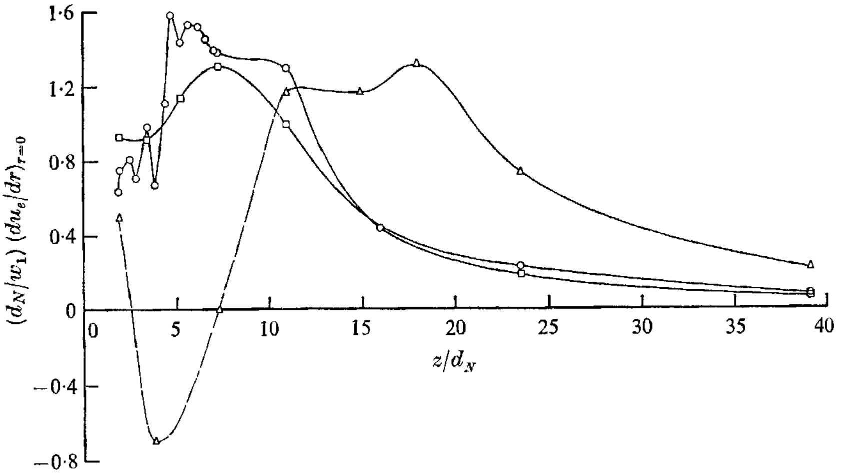

FIGURE 24. Variation of stagnation point non-dimensional radial velocity gradient with impingement distance for several pressure ratios. Flat plate, $\alpha = 90°$. Values of p_∞/p^0 (or p_1/p_∞): □, 0·800 (1·00); ○, 0·372 (1·42); △, 0·148 (3·57).

The non-dimensional gradient based on local free jet properties (figure 25) appears to achieve a rough correlation of the measured results, although the core effects of the strongest jet are still in evidence. In general, the two weakest jets are well correlated about a value $(r_5/w_c)(du_e/dr)_{r=0} \approx 1{\cdot}1$ for a considerable distance. Far downstream, the strongest jet also approaches this value.

The effect on the correlation of curvature of the impingement surface is shown in figure 26, where only the values representing impingement of fully developed portions of the jet are included. The relation

$$\frac{r_5}{w_c}\left(\frac{du_e}{dr}\right)_{r=0} \approx 1{\cdot}13 + 1{\cdot}08\frac{r_5}{r_S} \qquad (2)$$

represents the data quite well for $-0{\cdot}7 < r_5/r_S < 0{\cdot}7$ where r_S is the surface radius of curvature which is negative for a concave surface.

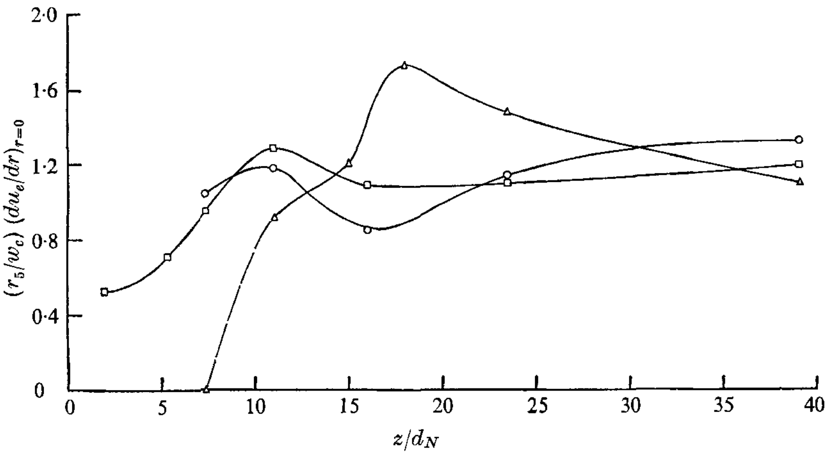

FIGURE 25. Variation of stagnation point non-dimensional radial velocity gradient with impingement distance for several jet pressure ratios. Flat plate, $\alpha = 90°$. Values of p_∞/p^0 (or p_1/p_∞): □, 0·800 (1·00); ○, 0·372 (1·42); △, 0·148 (3·57).

For oblique impingement, values of the non-dimensional form

$$\frac{r_5}{w_c}\left[\left(\frac{du_e}{dr}\right)_{r=0}\right]_1$$

are plotted in figure 27. In this figure, the cases for which core effects were large ($z/d_N = 1{\cdot}96$) are shown separately. While there is considerable spread in the remaining cases, it should be noted that the evaluation of $(r_5/w_c)\,[(du_e/dr)_{r=0}]_1$ for oblique impingement was inherently more difficult than it was for the normal impingements because of lower resolution obtained in the pressure distributions. In general, for $z/d_N = 23{\cdot}5$ and $39{\cdot}1$, there is only a slight change for $90° \geqslant \alpha \geqslant 75°$ and a moderate drop-off for $\alpha < 75°$. At $z/d_N = 7{\cdot}32$, the drop between $\alpha = 90°$ and $75°$ is quite distinct, which may be due to the sharper velocity profile near the end of the core. A curve

$$\frac{r_5}{w_c}\left[\left(\frac{du_e}{dr}\right)_{r=0}\right]_1(\alpha) = \frac{r_5}{w_c}\left[\left(\frac{du_e}{dr}\right)_{r=0}\right]_1(\alpha = 90°)\sin\alpha \qquad (3)$$

is plotted which gives a reasonable representation of the general behaviour. This might be expected if one considers that the pressure distributions remain essentially constant in characteristic breadth and only the component of total momentum flux normal to the surface is destroyed. For the case of $\alpha = 90°$, a value of

$$\frac{r_5}{w_c}\left[\left(\frac{du_e}{dr}\right)_{r=0}\right]_1 = 1{\cdot}13 \tag{4}$$

is used, based on the correlation of higher accuracy normal impingement data.

3.2.5. *Azimuthal distribution of the wall jet: basic characteristics.* The turbulent wall jet régime has been described earlier as that portion of the flow in which the effects of interaction due to impingement are no longer important. As such,

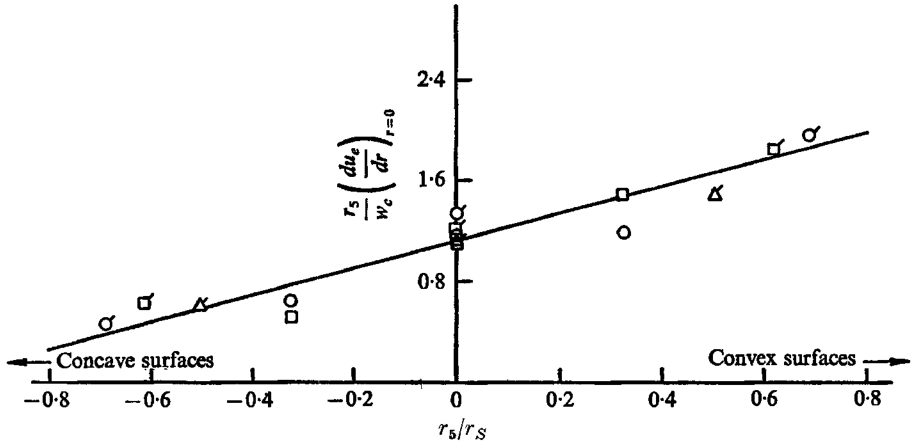

FIGURE 26. Dependence of non-dimensional radial velocity gradient on surface shape.

p_∞/p^0	z/d_N 23·5	z/d_N 39·1
0·800	□	□́
0·372	○	○́
0·148		△́

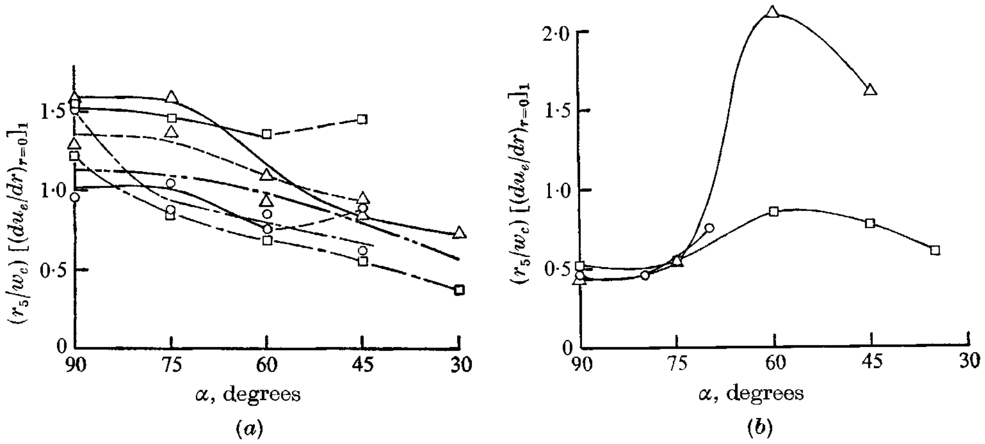

(a) (b)

FIGURE 27. Dependence of non-dimensional radial velocity gradient on angle of impingement. —· ·—, curve of equation (3), (a) z/d_N: —·—, 7·32; ——, 23·5; ---, 39·1. (b) $z/d_N = 1{\cdot}96$. p_∞/p^0: □, 0·800; ○, 0·372; △, 0·148.

it consists of an inner, boundary-layer-like region adjacent to the plate, with an outer layer of free turbulent mixing.

Because of the differences in the processes governing the growth of the two layers, the wall jet that results when the two layers are combined cannot establish a characteristic self-similar velocity profile. Glauert (1956) has shown that for an incompressible flow this departure from similarity is very slight, there being a tendency for the boundary layer to grow somewhat more rapidly in proportion to the overall profile growth. It is shown that the decay and spreading parameters which govern the combined growth rate are dependent upon the local Reynolds number of the flow. Typically, for the present flows in which the Reynolds number based on wall jet thickness ranges from 10,000 to 200,000, Glauert's results predict a velocity decay proportional to $r^{-1\cdot 1}$ with a thickness increase proportional to $r^{1\cdot 01}$.

One of the important characteristics of the radial wall jet produced by an impinging jet is the azimuthal distribution of the total mass flux when the impingement is oblique. Since the radial fluxes of momentum and energy per unit azimuth depend upon this distribution, it is particularly important if one is interested, say, in the local heat transfer between such a jet and a surrounding wall or enclosure. Certain characteristics of the flow appear to be obvious, such as the increasing proportion of mass flux in the downstream direction as α is made smaller. On the basis of inviscid theory, one might also expect a tendency toward a corresponding increase in thickness. However, the actual roles of real effects such as turbulent mixing, stagnation point displacement, non-radial flow components, and the nature of the impinging jets have to be deduced from the experimental data.

3.2.6. *Wall jet measurements.* The experimental programme consisted of the measurement of Pitot pressure profiles in the wall jet at several azimuthal positions ϕ along the perimeter of the flat, circular, impingement plate for a number of combinations of jet strength, axial location, and impingement angle. Velocities were computed from the Pitot pressure by assuming a constant static pressure equal to ambient. Measurements were made for one jet strength (moderately under-expanded, $p_\infty/p^0 = 0\cdot 372$) at each of five axial locations and five jet strengths at a single axial location ($z/d_N = 7\cdot 32$). For each of these combinations, the profile was determined for impingement angles α between 90° and 45°.

Several typical measured profiles are shown in figure 28, plotted in non-dimensional form with the maximum velocity $u_{\max}$ and the half-velocity thickness normal to the plate n_5 as normalizing parameters. The case for $\alpha = 60°$, $\phi = 180°$ represents the greatest deviation from the typical measured profile exemplified by the other two cases. A single curve which represents a good fit for all of the measured profiles is shown in figure 29, together with a curve based on Glauert's analysis. In order to select a theoretical curve for comparison with the data, the boundary-layer thickness, i.e. the thickness to $u_{\max}$, was made to coincide with the experimental result and the outer profile was passed through the point $n = n_5$. The resulting curve coincides with a distribution obtained from Glauert's results for a Reynolds number $u_{\max}\delta/\nu = 13{,}000$ where δ is the half-velocity thickness of the outer layer only (distance between points for $u_{\max}$ and

$0{\cdot}5u_{\max}$). This Reynolds number is representative of profiles near the low end of the range of Reynolds numbers (10,000 to 200,000) covered by the data. Since a Glauert profile for a Reynolds number of 200,000 has a significantly thinner inner layer than was measured in these tests, it is concluded that the present data show somewhat less Reynolds number dependence than would be predicted by Glauert's analysis.

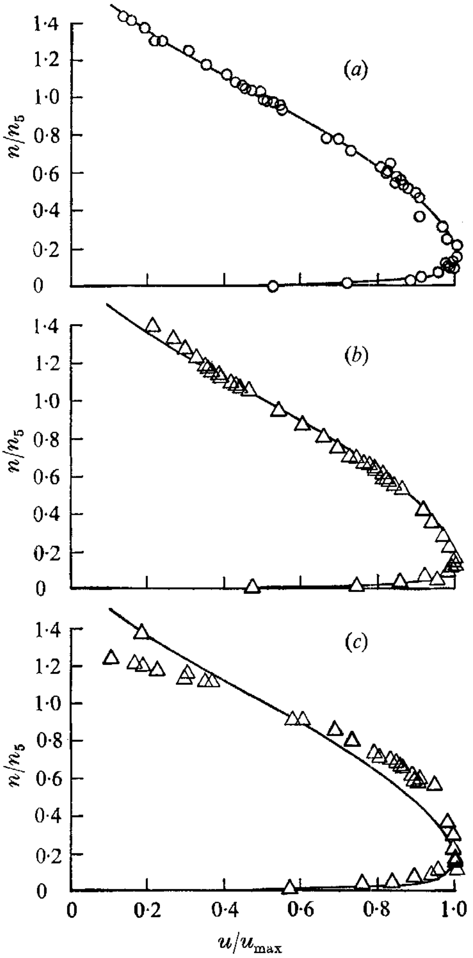

FIGURE 28

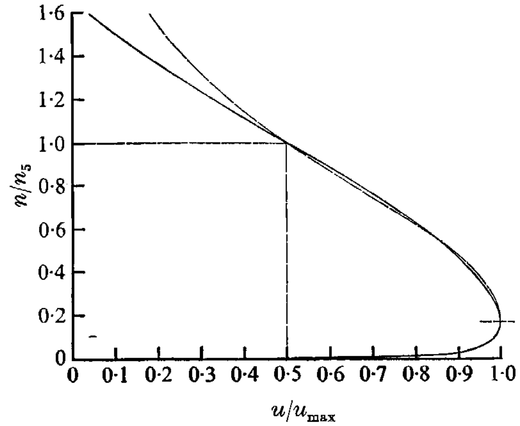

FIGURE 29

FIGURE 28. Wall jet velocity profiles for several different impingement conditions. The curve is the experimental data curve shown in figure 29. $z/d_N = 7{\cdot}32$; $p_\infty/p^0 = 0{\cdot}372$. (a) $\alpha = 90°$, $\phi = 0°$; (b) $\alpha = 60°$, $\phi = 0°$; (c) $\alpha = 60°$, $\phi = 180°$.

FIGURE 29. Comparison of experimental curve with that based on Glauert's theory. — —, Glauert (1956); —— curve based on experimental measurements.

Results which typify the maximum velocity and thickness values measured are presented in figures 30 to 33. The maximum velocities given are referred to their values at $\phi = 0$ for each impingement condition. Values of $(u_{\max})_{\phi=0}$ are given in figure 31 in terms of the parameters governing the impingement condition, i.e. the free jet centreline velocity w_c, the half-velocity radius r_5 measured at the impingement distance, and the plate wetted radius r_w.

The azimuthal variation of $u_{\max}/(u_{\max})_{\phi=0}$ is relatively independent of impingement condition for the range of cases studied, and the curves of figure 30 are quite typical. Because of the large range in velocity magnitudes, however, the margin of experimental error for each curve is variable, with larger errors

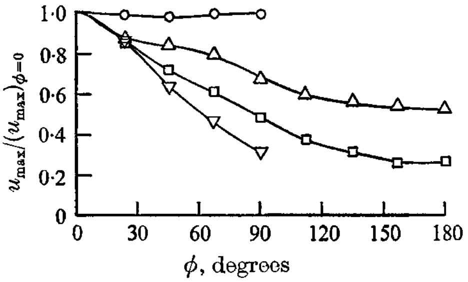

FIGURE 30. Dependence of wall jet non-dimensional maximum velocity on azimuthal position. $p_\infty/p^0 = 0{\cdot}372$; $z/d_N = 7{\cdot}32$. Values of α: ○, 90°; △, 75°; □, 60°; ▽, 45°.

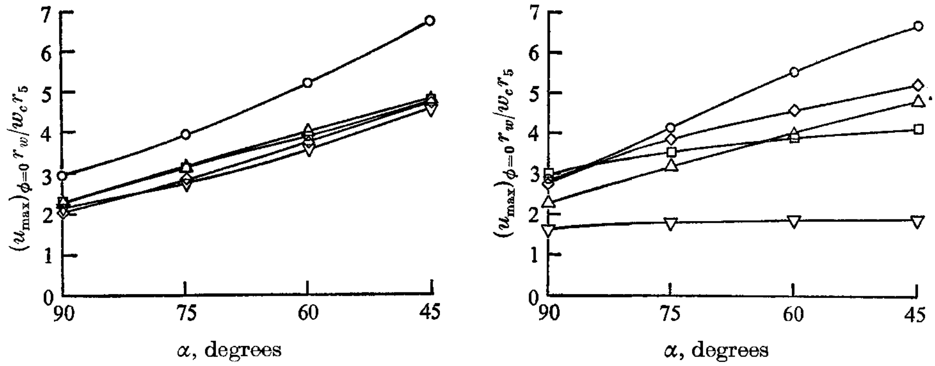

(*a*) (*b*)

FIGURE 31. Non-dimensional wall jet maximum velocity at $\phi = 0$ as a function of impingement angle. (*a*) $z/d_N = 7{\cdot}32$. p_∞/p^0: ○, 0·148; △, 0·372; ▽, 0·458; ◇, 0·552; □, 0·800. (*b*) $p_\infty/p^0 = 0{\cdot}372$. z/d_N: ○, 1·96; △, 7·32; ◇, 11·7; □, 23·5; ▽, 39·1.

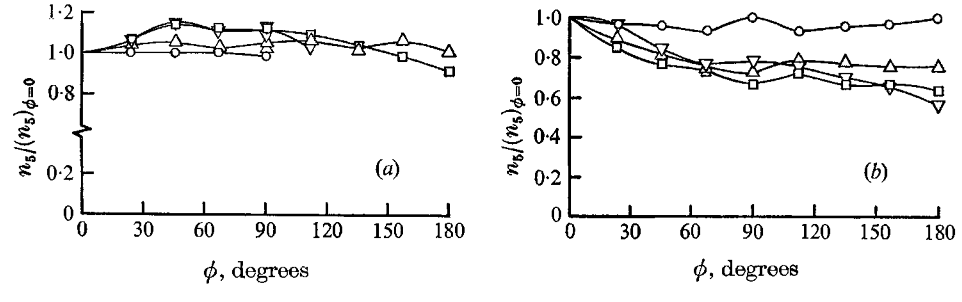

FIGURE 32. Dependence of wall jet non-dimensional thickness on azimuthal position. (*a*) $p_\infty/p^0 = 0{\cdot}372$, $z/d_N = 7{\cdot}32$. (*b*) $p_\infty/p^0 = 0{\cdot}372$, $z/d_N = 1{\cdot}96$.

to be expected for lower velocities. For some cases, of course, such as the two axial stations farthest downstream, it is doubtful that a well-formed wall jet existed at all at the edge of the plate. For $z/d_N = 23{\cdot}5$ and $39{\cdot}1$, the values of r_5 for the impinging jets are about $0{\cdot}21r_w$ and $0{\cdot}44r_w$, respectively. Allowing for the extent of the full jet profile, it is clear that the edge of the plate would not be far removed from the impingement interaction régime. In this connexion, it should be mentioned that a check for non-radial components in the r, ϕ plane was made for several extreme conditions of ϕ and α using the direction-sensitive probe mounted on the rake. It was found that no significant components existed in these cases.

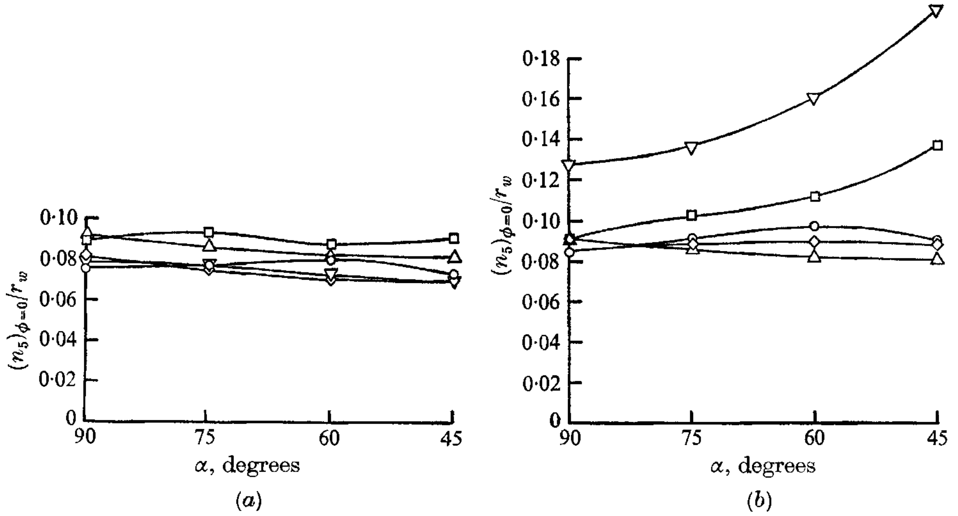

FIGURE 33. Non-dimensional wall jet thickness at $\phi = 0$ as a function of impingement angle. (a) $z/d_N = 7{\cdot}32$. p_∞/p^0: ○, 0·148; △, 0·372; ▽, 0·458; ◇, 0·552; □, 0·800. (b) $p_\infty/p^0 = 0{\cdot}372$. z/d_N: ○, 1·96; △, 7·32; ◇, 11·7; □, 23·5; ▽, 39·1.

The most striking feature of the behaviour of the thickness parameter n_5 is its relative invariance with both α and ϕ. In figure 32, $n_5/(n_5)_{\phi=0}$ is plotted *versus* ϕ, while the values of $(n_5)_{\phi=0}$ are given in figure 33, in which they are related to the plate radius r_w. The lack of any significant azimuth dependence is indicative of the effect of turbulent mixing in governing these flows. It is apparent that, regardless of the momentum level of each azimuthal sector of the wall jet, the spreading rate is very nearly the same for all sectors. This is so because the local shear stress which effectively produces the spread and decay is itself proportional to the local momentum level. Thus, a weak portion of the wall jet (e.g. in the upstream direction) spreads just as rapidly as a strong portion (e.g. in the downstream direction). As in the case of other flows with turbulent mixing, of course, a weak dependence upon Mach number might be expected. It is possible that the slight tendency toward increased thickness with increasing ϕ in some cases may be due to such an effect since spreading rates are greater for lower Mach numbers.

Azimuthal distributions of radial momentum flux were determined from the measured velocity profiles by graphical integration based on the curve in figure 29.

Typical results are shown in figure 34, in which the ratio of momentum flux per radian to its average value for $\alpha = 90°$ is plotted as a function of ϕ. As expected, the general behaviour is similar in all cases, with a tendency toward less variation with ϕ for increasing impingement distance. For a fixed impingement distance,

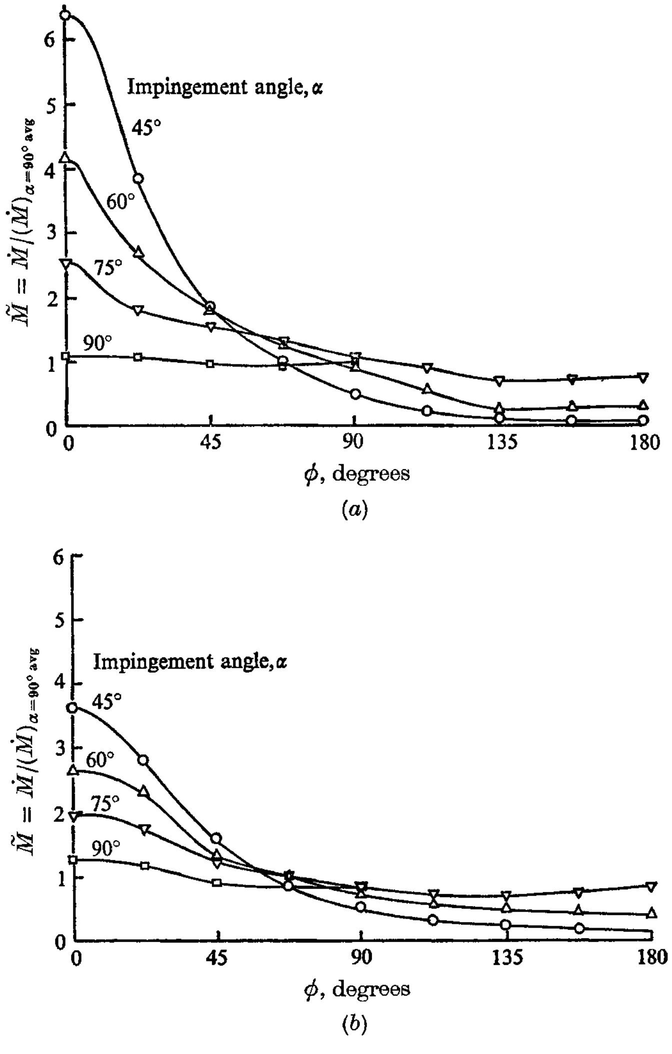

FIGURE 34. Azimuthal variation of measured wall jet momentum flux. (*a*) $p_\infty/p^0 = 0{\cdot}372$, $z/d_N = 1{\cdot}96$. (*b*) $p_\infty/p^0 = 0{\cdot}372$, $z/d_N = 23{\cdot}5$.

little effect of jet strength was found except in the case of the highly under-expanded jet which showed a higher concentration of momentum flux near $\phi = 0$.

The characteristic azimuthal momentum distributions just described and the observed behaviour of the wall jet thickness described earlier suggest a useful way to understand the distribution of radial fluxes for such oblique flows in general. The radial flow is thought of as divisible into sectors or 'pie-shaped' pieces. If it is assumed that momentum and energy exchange between adjacent sectors is negligible, then the development (i.e. spread and decay) of each sector as it is followed radially outward should depend primarily on the initial unit momentum flux per radian for that sector. This initial unit flux, of course, would be that produced by the normal impingement of a jet of suitable strength. As a consequence of this independent development, it would be expected that the unit momentum flux of each sector would be conserved in the radial direction. If this were so, it would be possible to predict the momentum distribution at any radial station using known values for a single radial station.

In order to test this hypothesis, additional velocity profiles were measured for a typical impingement condition with plates having radii equal to 1·5 and 2·0 times the basic plate radius. The profile shape at each radius was first checked in detail at $\phi = 0°$ for $\alpha = 45°$ and $90°$. These profiles all appeared to be similar, both to each other and to the profile already established (figure 29). Thus, the same basic non-dimensional velocity profile was assumed to apply for all three plate sizes. In addition, the wall jet was assumed to be incompressible for the two larger plates. Under these conditions, the integral expression for the radial momentum flux per radian around the plate can be written

$$\begin{aligned}\dot{M}(\phi) &= \rho u_{\max}^2 r_w n_5 \int_0^\infty \left(\frac{u}{u_{\max}}\right)^2 d\left(\frac{n}{n_5}\right) \\ &= \rho u_{\max}^2 r_w n_5 I_{wj},\end{aligned} \tag{5}$$

where I_{wj} is evaluated uniquely from the basic wall jet profile. If the momentum loss in the boundary layer is neglected, it can then be shown that wall jet momentum is conserved if the product $u_{\max}^2 r_w n_5$ is invariant with r_w.

Values of n_5 and $u_{\max}$ were measured for a range of the impingement angle at $\phi = 0°$ and $180°$ for the given impingement condition. These values are plotted against r_w/r_{w_1} in figure 35, in which n_5 is given in the non-dimensional form n_5/r_w and $u_{\max}$ is made non-dimensional by means of the local impinging jet parameters $w_c r_5$; the quantity r_{w_1} is the radius of the smallest plate.

When the momentum coefficient $u_{\max}^2 r_w n_5$ is computed from the measured data, it is found to be very nearly independent of r_w. These values are plotted at the bottom of figure 35. On the basis of these results, it appears that the two wall jet sectors in question ($\phi = 0°$ and $180°$) were in no way coupled to their neighbouring sectors. In addition, this conclusion holds true regardless of changes in momentum level produced by variation of the impingement angles.

In view of the observed momentum conservation for two wall jet sectors, a similar condition may be inferred for the remaining sectors if it is assumed that for a given impingement angle the azimuthal distribution of momentum flux per radian established earlier for the smallest plate (figure 34) remains the same at larger radii. If changes in the distribution of shearing stresses within the wall jet are neglected, the primary cause for any apparent change in this distribution of $\dot{M}(\phi)$ would be the failure to allow for non-radial velocity components in the measured profiles. Since such components were found to be negligible for the smallest radius, it is felt that the assumption of sector independence is physically reasonable.

3.3. *Special study of stagnation region flow*

The pressure distributions measured for impingement distances just downstream of the normal shock disk in the highly under-expanded jet show that the peak of maximum Pitot pressure observed in the free jet to either side of the centreline is still present. A typical example of such a distribution along with the Pitot and static pressure profiles in the free jet at the same axial distance is shown in figure 36. The persistence of this outer peak when impingement occurs suggests the existence of a separated region caused by the reversed pressure gradient between the outer peak and the centreline. This condition accounts for the negative values of $(du_e/dr)_{r=0}$ mentioned before. The flow pattern based on this idea is shown in figure 37. The usual central stagnation point is transformed into a ring surrounding the separated region. A pattern similar to this is known to exist under certain ground effects machines. A consequence of such a flow

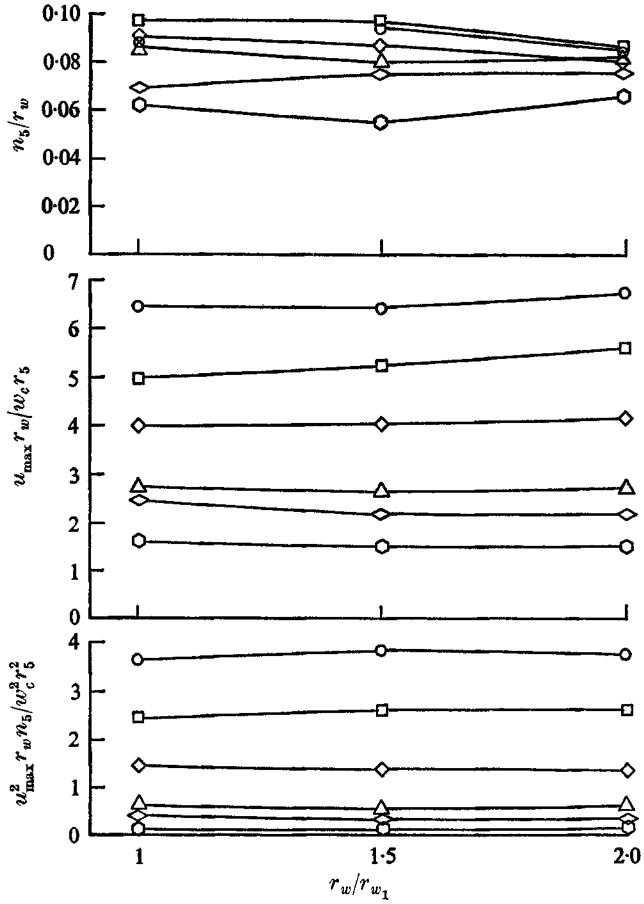

FIGURE 35. Dependence of wall jet characteristics on radial location. $p_\infty/p^0 = 0{\cdot}372$; $z/d_N = 1{\cdot}96$. Values of α (and ϕ): ○, 45 (0); □, 60 (0); ◇, 75 (0); △, 90(0); ⬯, 60 (180); ◇, 75 (180); △, 90 (180).

in terms of heat transfer, say, from a hot jet to a cold surface, would be the existence of a cool central spot surrounded by a ring at stagnation point heating levels.

Since direct measurement of velocity or pressure gradients off the surface was felt to be impossible, a method was devised for confirming the pattern by observing surface streamlines. This method consisted of impinging the jet for a short time on a layer of a highly viscous mixture of water-pump grease and lamp-black applied to the surface of the flat plate. Maximum visual contrast was achieved by giving the plate a smooth finish of white lacquer. It was found that the initial distribution or thickness of the grease did not affect the resulting pattern. With the grease applied in a small blob, the plate was covered with a baffle board in order to shield the grease from transient phenomena during the starting and stopping of the jet. When the jet reached the desired running condition, the baffle was withdrawn for a short time interval of about 3 to 5 sec. The baffle was then replaced. A photograph of this pattern for the highly under-expanded jet at $z/d_N = 5{\cdot}32$ is shown in figure 38 (plate 4). The behaviour of surface streamlines suggested by the observed patterns is shown schematically

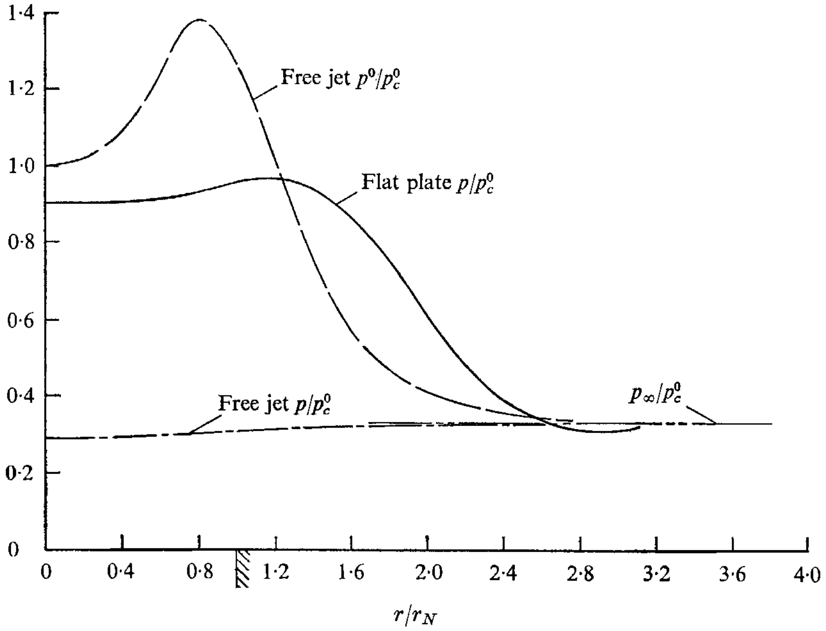

FIGURE 36. Comparison of measured pressure distributions on flat plate and in free jet. $p_\infty/p^0 = 0{\cdot}148$; $p_1/p_\infty = 3{\cdot}57$; $z/d_N = 7{\cdot}32$.

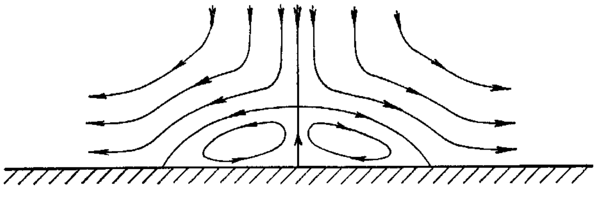

FIGURE 37. Flow pattern of separated region (distance normal to surface exaggerated).

in figure 39. It is seen that a dividing ring exists which separates regions of inward and outward flow. To the inside there is a central region of thick grease, while to the outside an alternating concentric pattern of more and less grease is observed. Of particular interest is the manner in which the streaks curve near the dividing ring, resulting in segmentation of the central pattern. Along the dividing ring, each segment can be identified by two types of points having the topological character of nodes 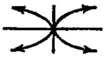 and saddle points 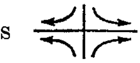. The number of segments in the pattern was found to decrease with increasing impingement distances. A minimum number of three segments was observed for all distances beyond about $z/d_N = 4{\cdot}5$. Another factor which was found to affect not only the number of segments at a given distance but also the orientation of the pattern was the jet nozzle. Rotation of the nozzle about its axis between runs resulted in an identical rotation of the observed grease pattern. It was found that tiny nicks in the nozzle lip could be correlated with at least some of the pattern segments. Removal of the larger nicks resulted, for impingement distances less than 4·5, in fewer segments. The patterns shown in the present case are those resulting from tests after the nicks had been removed from the nozzle. Under 10-power magnification, no nicks were observed that could be correlated with the resulting three equal pattern segments. Thus it appears that the three-segment pattern represents a stable form of the trapped 'bubble' of separated flow, with its orientation determined by the position of microscopic flaws in the nozzle lip.

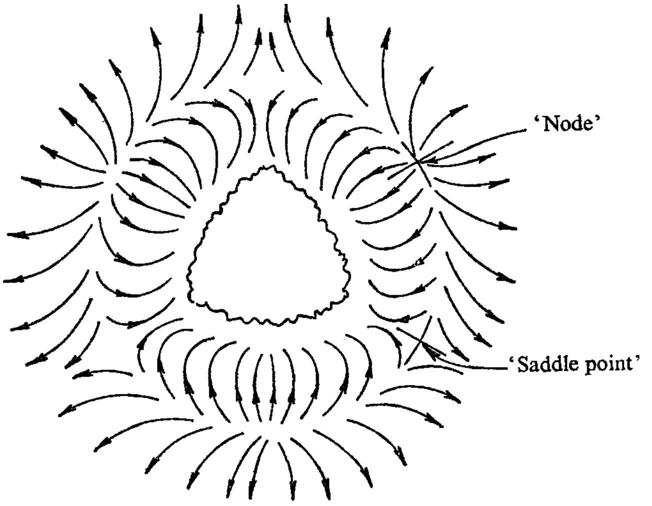

FIGURE 39. Typical surface streamline pattern based on grease streak pictures.

A comparison of schlieren photograph, grease pattern, and surface pressure distribution for a typical case is shown in figure 40 (plate 5). It can be seen that local pressure peaks are definitely related to the observed patterns, with less grease remaining where the pressure is higher. These local pressure maxima also correspond to the dark regions of increasing density near the surface shown in the schlieren picture. The pressure peaks do not correspond, however, with the location of the dividing ring which falls somewhat inside of the peaks.

4. Concluding discussion

The work which has just been reviewed is the first part of an extensive study of free jet impingement. The overall aim of this study is an understanding of jet impingement heat transfer. In the first part, the investigation has been devoted primarily to the behaviour of free jets when they impinge on surfaces of several shapes at various impingement angles. In particular, the general character of the stagnation point radial velocity gradient $(du_e/dr)_{r=0}$ has been delineated. Knowledge of this gradient is important to the calculation of heat transfer at the stagnation point.

The primary flow studied was a subsonic, axially symmetric jet of pressure ratio $p_\infty/p^0 = 0{\cdot}800$ ($M_1 = 0{\cdot}57$). (This same type of flow was used for the direct measurement of impingement heat transfer to be reported in part 2 of this study.) In addition to the subsonic jet, however, the present paper has described the impingement behaviour of two additional types of flow from the same convergent nozzle—one slightly under-expanded ($p_\infty/p^0 = 0{\cdot}372$) and one highly under-expanded ($p_\infty/p^0 = 0{\cdot}148$). Each of the three types of jet impinged normally on four different surfaces: a flat plate, a convex hemisphere, a concave hemisphere, and a cylindrical cup. In addition, the effect of obliqueness of impingement was investigated with the flat plate at impingement angles between 45° and 90°. Values of the stagnation-point radial velocity gradient were computed from the pressure distributions measured for each combination of jet strength, impingement distance and angle, and surface shape.

The results of the studies of $(du_e/dr)_{r=0}$ for normal impingement were presented in two-dimensional forms. In the first form, the parameter was made dimensionless using the jet exit diameter and jet exit velocity, i.e.

$$\frac{d_N}{w_1}\left(\frac{du_e}{dr}\right)_{r=0}.$$

This form is useful for quick estimates of $(du_e/dr)_{r=0}$ when information is not available concerning the decay of the free jet under consideration. The other non-dimensional form attempts a correlation with local conditions in the free jet at the plane of impingement, i.e.

$$\frac{r_5}{w_c}\left(\frac{du_e}{dr}\right)_{r=0}.$$

The data show that such a correlation is useful in the region of fully developed free jet flow. In particular, for the case of normal impingement on a flat plate

$$\frac{r_5}{w_c}\left(\frac{du_e}{dr}\right)_{r=0} \approx 1{\cdot}13.$$

The effect of curvature of the impingement surface on the stagnation point radial velocity gradient was found for fully developed jets to be approximated by the relation

$$\frac{r_5}{w_c}\left(\frac{du_e}{dr}\right)_{r=0} \approx 1{\cdot}13+1{\cdot}08\frac{r_5}{r_S}$$

for $-0{\cdot}7 < r_5/r_S < 0{\cdot}7$ where r_S is the surface radius of curvature which is negative for a concave surface.

For oblique impingement, the correlation of values of $[(du_e/dr)_{r=0}]_1$ with local free jet conditions was found to be somewhat inconsistent. In general, however, a decreasing trend was noted in the value of the non-dimensional form

$$(r_5/w_c)/[(du_e/dr)_{r=0}]_1$$

as obliqueness increased for all the jets at all but the closest impingement distance. For $90° \geqslant \alpha \geqslant 75°$ at $z/d_N = 1{\cdot}96$, non-dimensional values correlated quite well, while the behaviour for $\alpha < 75°$ showed peaks of different magnitudes near $\alpha = 60°$.

The effects of obliqueness on the impingement pressure distributions themselves were found to be generally similar for all three jets at all axial stations except the closest ($z/d_N = 1{\cdot}96$). These effects were characterized by changes in the stagnation-point pressure level and a shift in its position on the plate surface. For the downstream stations representing impingement of essentially fully developed jet velocity profiles, the stagnation point pressure was relatively insensitive to impingement angle in the range $90° \geqslant \alpha \geqslant 75°$. For smaller angles, the observed drop-off became nearly linear. The overall behaviour was roughly dependent on $\sin^2\alpha$. For impingement of the jet core, little change in pressure level was noted until α was decreased below 60°. The shift of the stagnation point also followed a similar pattern. Downstream locations showed a fairly linear change with α in the range $90° \geqslant \alpha \geqslant 60°$. At $z/d_N = 1{\cdot}96$, a higher rate of change was generally observed through the entire α range. It is apparent that the different behaviour observed for core impingement is due to the flat velocity profile in that portion of the free jet.

The azimuthal distribution of the wall jet was found to be essentially as expected, with more mass and momentum flux concentrated near $\phi = 0$ for increased obliqueness (decreased α). Distributions of radial momentum flux per radian revealed little difference among the impingement conditions except far downstream where there was less dependence on ϕ for a given α. At a fixed distance, the flux of the highly under-expanded jet tended to be more concentrated near $\phi = 0$ than that of the weaker jets.

Wall jet velocity profiles were characterized by their maximum velocities $u_{\max}$ and half-velocity thicknesses n_5. Similar results were obtained under all conditions except, again, for stations far downstream. In general, $u_{\max}$ dropped off more rapidly with ϕ for smaller values of α, whereas n_5 was found to be relatively independent of both ϕ and α. Variations from the general behaviour for downstream locations were felt to be at least partly the result of the large extent of the impingement régime relative to the plate size. Under these conditions, it is doubtful if a fully developed wall jet was formed at the point of measurement.

Measurements of the wall jet velocity profile at two larger radii indicated that, for the wall jet sectors involved ($\phi = 0°$ and $180°$), the decay behaviour was virtually independent of that in the neighbouring sectors.

In order to evaluate the non-dimensional stagnation point radial velocity gradient $(r_5/w_c)\,(du_e/dr)_{r=0}$, the local properties of a given jet downstream of its point of issuance must be known. In the present case, measurements of these properties (r_5 and w_c) were made over a wide range of conditions including those for which the impingement studies were done. It was observed that secondary effects, such as a 'flapping' instability, were present. In addition, a simple blockage test was made in which a baffle plate surrounding the nozzle exit was found to have a significant effect on the impingement pressure distribution. Because of the apparent sensitivity of jet impingement flows to such secondary effects, it was concluded that values of r_5 and w_c used to correlate jet impingement data should be measured under the same experimental conditions as those used for the impingement measurements themselves.

With the correlation established, the necessary values of r_5 and w_c for a given point in a given jet can be computed by means of one of the standard analytical techniques, such as the method due to Donaldson & Gray (1966). This method, which is an extension of the momentum integral technique of Warren (1957) and which makes use of a turbulent exchange coefficient based on local rather than initial conditions, has been applied successfully to the cases of subsonic, properly expanded, and improperly expanded jets with shocks for a wide range of stagnation enthalpies.

For the special case of a highly under-expanded jet ($p_\infty/p^0 = 0{\cdot}148$) containing a normal shock disk and impinging on a surface at close range ($z/d_N \leqslant 8$), an apparent region of separated flow exists surrounding the stagnation point. A study of surface streamlines suggests that, within this region, the radial flow is inward towards the stagnation point and that the maximum positive radial velocity gradient occurs along a ring surrounding this region.

This research was supported by the Advanced Research Projects Agency, Ballistic Missile Defense Systems Branch, and was monitored by the U.S. Naval Research Laboratory under Contract no. Nonr–3903(00)(X).

REFERENCES

ANDERSON, A. R. & JOHNS, F. R. 1955 *Jet Propul.* **25**, 13–15, 25.

ANDERSON, A. R., JOHNS, F. R. & HAWKES, W. M. 1954 *US NADC*-ED-5401.

D'ATTORE, L. & HARSHBARGER, F. 1964 *General Dynamics/Astronautics Report* GDA-DBE 64-008.

DONALDSON, C. DUP. & GRAY, K. E. 1966 *AIAA J.* **4**, 2017–2025.

GLAUERT, M. B. 1956 *J. Fluid Mech.* **1**, 625–643.

HAMMITT, A. G. 1961 *J. Aero. Sci.* **28**, 673–680.

HENDERSON, L. F. 1960 *Australian Defence Scientific Service, Mech. Engng Note* 238.

KRZYWOBLOCKI, M. Z. 1956 *Jet Propul.* **26**, 760–779.

LOVE, E. S., GRIGSBY, C. E., LEE, L. P. & WOODLING, M. J. 1959 *NASA TR* R-6.

Olson, R. E. & Miller, D. P. 1963 *United Aircraft Corp. Report* A-1771-24.

Owen, P. L. & Thornhill, C. K. 1952 *Aero. Res. Council R & M* 2616.

Reshotko, E. & Cohen, C. B. 1955 *NACA TN* 3513.

Seddon, J. & Haverty, L. 1956 *Aero. Res. Council C.P.* 246.

Snedeker, R. S. & Donaldson, C. duP. 1964 *Aero. Res. Associates of Princeton, Inc. Report* 63.

Snedeker, R. S. & Donaldson, C. duP. 1965 *Aero. Res. Associates of Princeton, Inc. Report* 64.

Stitt, L. E. 1961 *NASA TN* D-1095.

Warren, W. R. 1957 *Princeton Univ. Aero. Engng Dept. Report* 381.

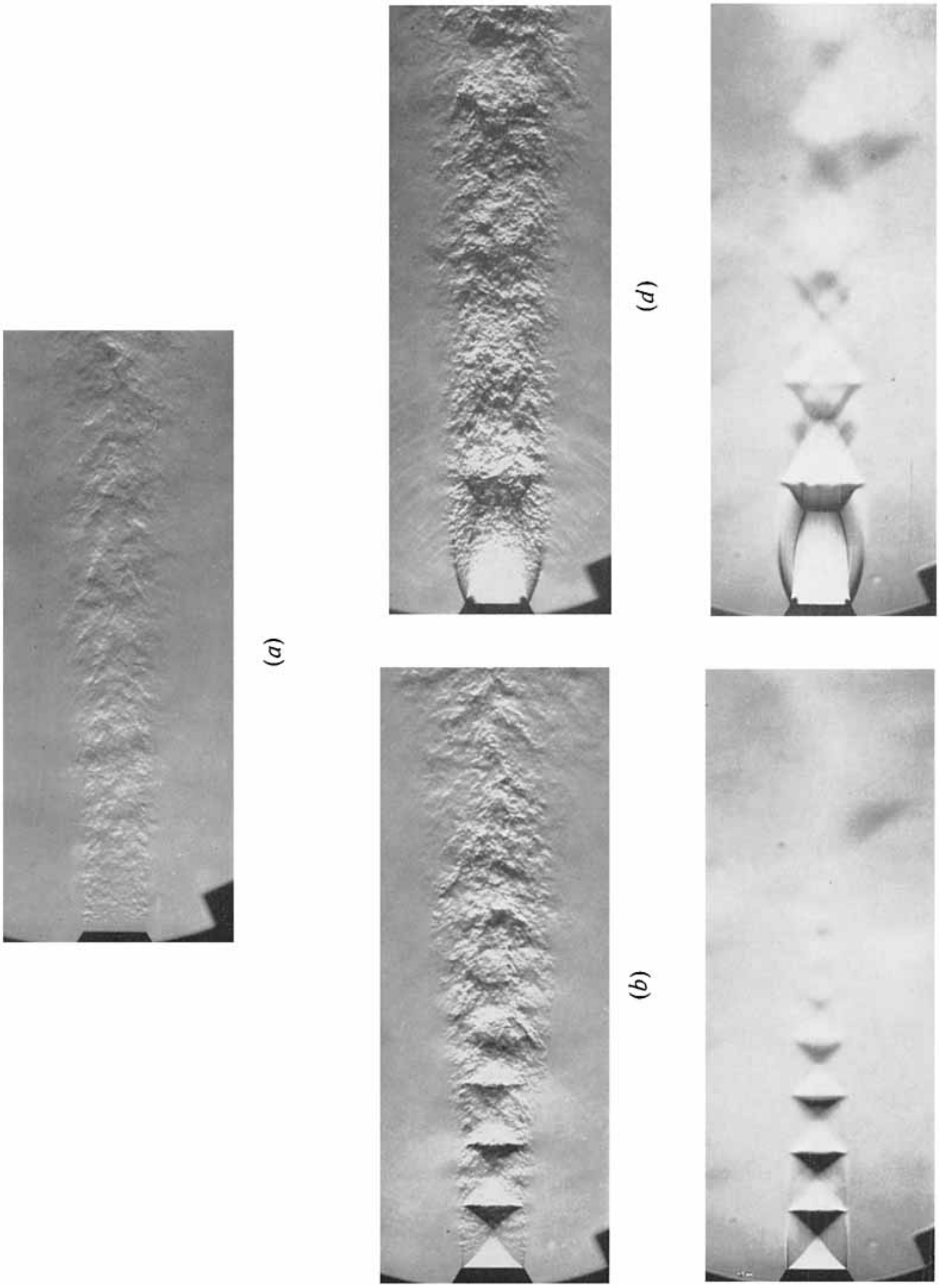

FIGURE 2. Schlieren photographs of typical jet types shown in figure 1. (*a*) Spark light, subsonic jet, $p_\infty/p^0 = 0{\cdot}552$. (*b*) Spark light and (*c*) continuous light, moderately under-expanded jet, $p_1/p_\infty = 1{\cdot}42$. (*d*) Spark light and (*e*) continuous light, highly under-expanded jet, $p_1/p_\infty = 3{\cdot}57$.

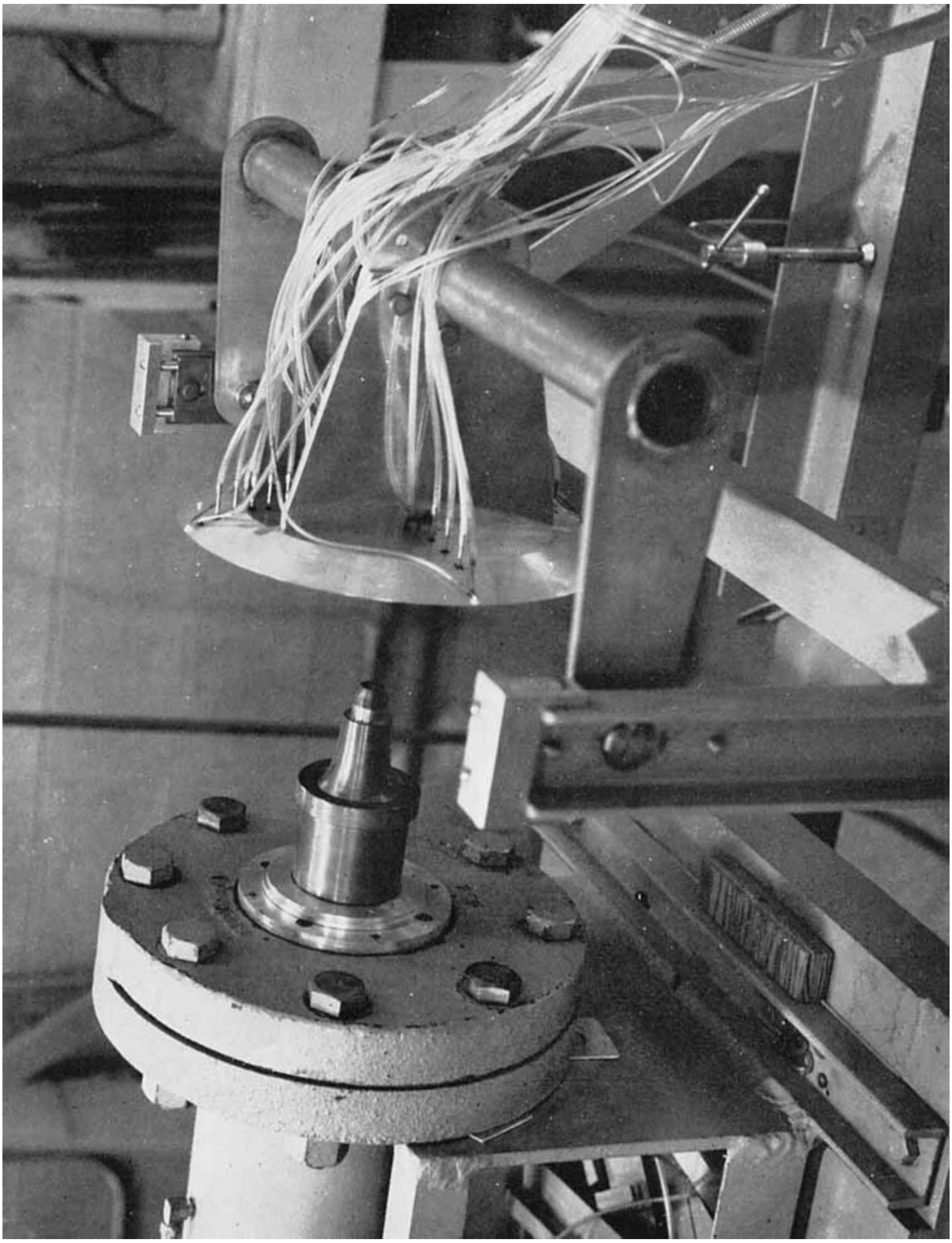

Figure 3. Nozzle and impingement model setup.

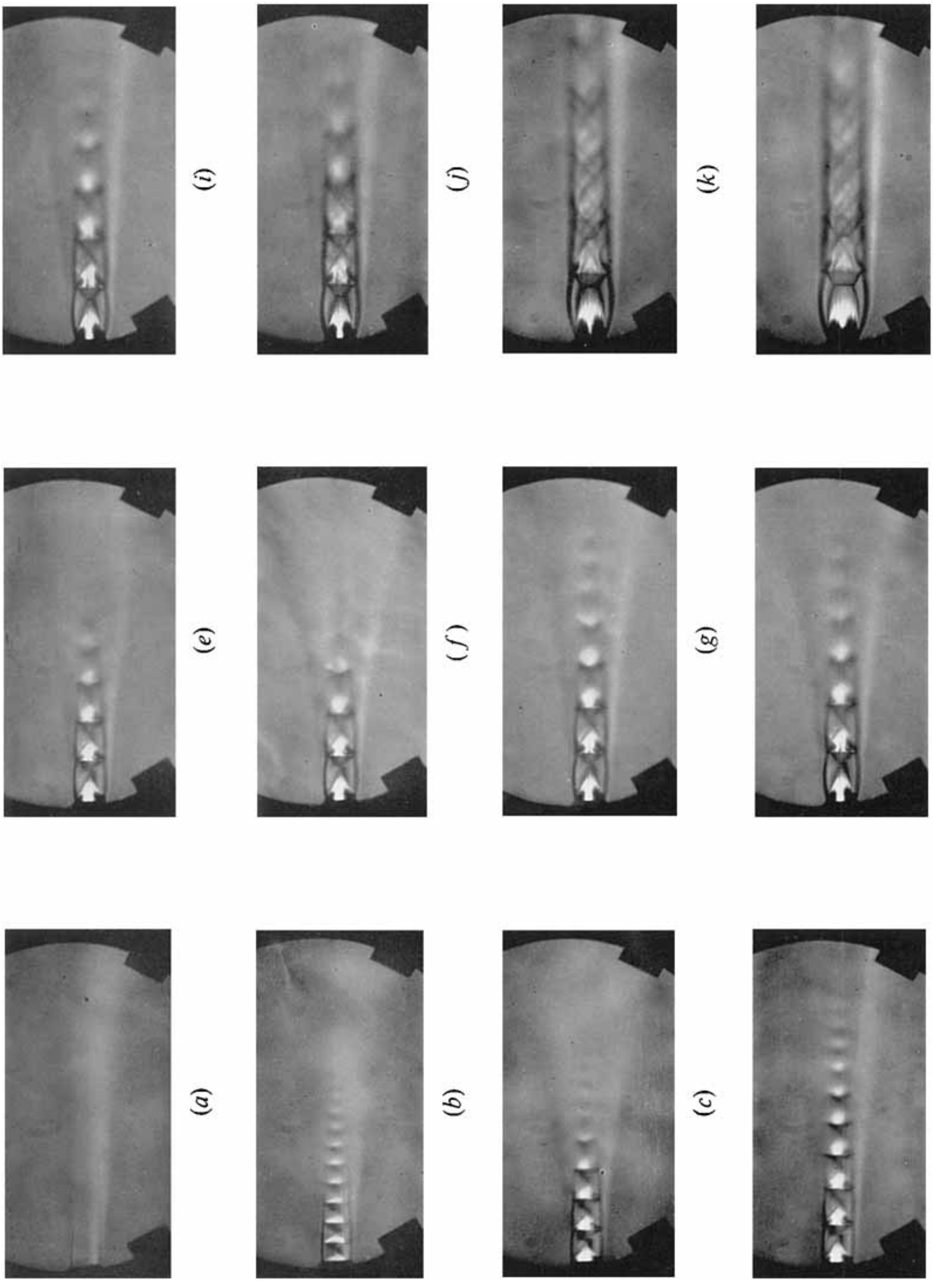

FIGURE 8. Free jet from convergent nozzle photographed with double-pass schlieren system. (*a*) $p_1/p_\infty = 1{\cdot}00$ (subsonic). (*b*) $p_1/p_\infty = 1{\cdot}15$. (*c*) $p_1/p_\infty = 1{\cdot}42$. (*d*) $p_1/p_\infty = 1{\cdot}59$. (*e*) $p_1/p_\infty = 1{\cdot}71$. (*f*) $p_1/p_\infty = 1{\cdot}84$. (*g*) $p_1/p_\infty = 2{\cdot}00$. (*h*) $p_1/p_\infty = 2{\cdot}13$. (*i*) $p_1/p_\infty = 2{\cdot}31$. (*j*) $p_1/p_\infty = 2{\cdot}59$. (*k*) $p_1/p_\infty = 3{\cdot}57$. (*l*) $p_1/p_\infty = 4{\cdot}09$.

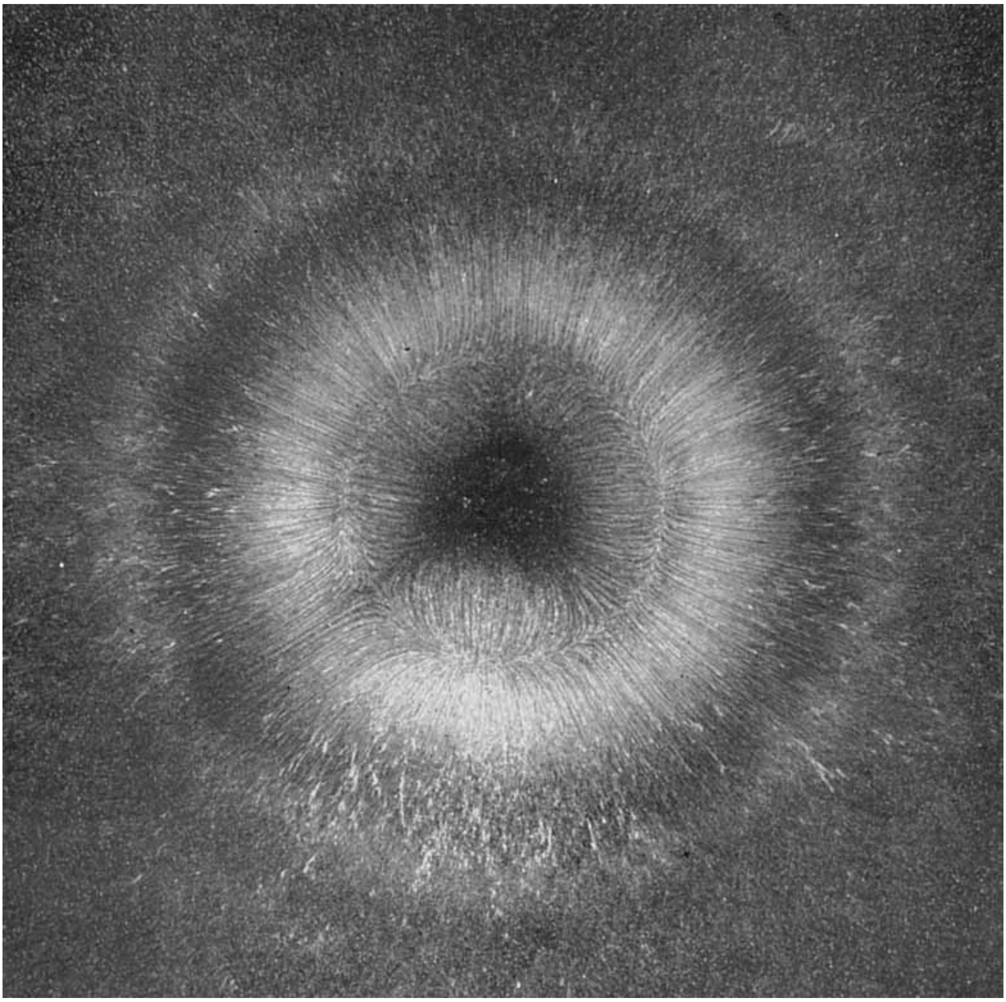

FIGURE 38. Typical grease streak photograph of flow pattern due to impingement on flat plate. $p_1/p_\infty = 3{\cdot}57$; $z/d_N = 5{\cdot}32$.

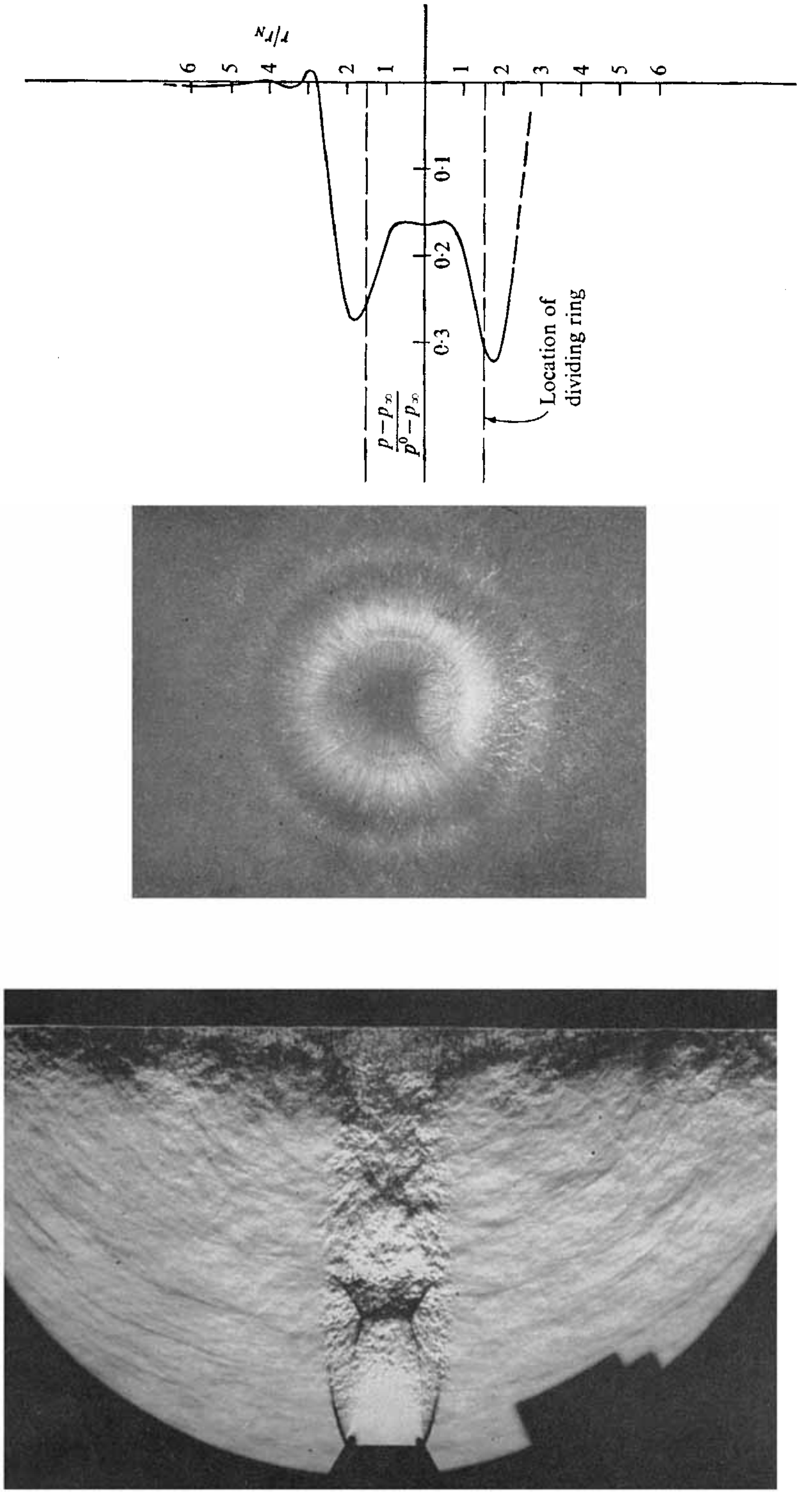

FIGURE 40. Typical jet impingement characteristics for a case in which a normal shock exists in the jet core. $p_1/p_\infty = 3{\cdot}57$; $z/d_N = 5{\cdot}32$.